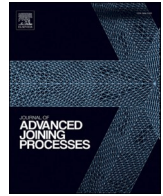


Contents lists available at [ScienceDirect](https://www.sciencedirect.com)

Journal of Advanced Joining Processes

journal homepage: www.sciencedirect.com/journal/journal-of-advanced-joining-processes

Comparative study of the effects of galvanic corrosion on the strength and the failure of aluminium and stainless steel bolted joints

Afaf Saai^{a,*}, Virgile Delhaye^a, Torstein Lange^b, Trond Furu^{c,d}, Kristian Aamot^e, John Lein^b

^a Materials and structural mechanics, Department of Materials and Nanotechnology, SINTEF Industry, NO-7465 Trondheim, Norway

^b Corrosion and Tribology, Department of Materials and Nanotechnology, SINTEF Industry, NO-7465 Trondheim, Norway

^c Norsk Hydro, Corporate Technology Office, Oslo, Norway

^d Norwegian University of Science and Technology, Department of Material Science and Engineering, Trondheim, Norway

^e Materials integrity and welding, Department of Materials and Nanotechnology, SINTEF Industry, NO-7465 Trondheim, Norway

ARTICLE INFO

Keywords:

Lap shear joint
Tensile-shear
Bimetallic inserts
Cyclic salt spray corrosion test
Digital image correlation
Finite element simulations

ABSTRACT

This paper investigates the effects of bimetallic insert on corrosion, material degradation, loading capacity, stress distribution, strain distribution and failure of aluminium-stainless steel lap shear bolted assemblies. The single bolt lap shear assemblies of aluminium and stainless steel plates were performed in two settings in one of them a bimetallic insert was used. Considering that the aluminium plays the role of sacrificial anode in the aluminium-stainless steel galvanic couple, a single bolt lap shear assembly joining two aluminium plates is also considered as a reference. The experimental measurements were determined by tensile-shear testing method for three different conditions: dry condition and two corrosion states corresponding to 6 weeks and 16 weeks of accelerated corrosion tests. To support understanding of the effects of preload and friction changes due to the formation of corrosion products, finite element simulations were performed with varying preloads and friction coefficients. The study demonstrated significant effects of corrosion on loading capacity, bolt rotation and failure mode. The tensile-shear forces measured for the aluminium-aluminium assembly and aluminium-stainless steel assembly after 6 weeks of accelerated corrosion tests increased compared to the tensile-shear forces measured in dry condition. The increase in tensile-shear forces was related to the formation of corrosion products, affecting the preload and the frictional behaviour of the contacting surfaces. In agreement with experimental observations, finite element simulations demonstrated an increase in the tensile-shear force with the increase of frictional forces. The application of bimetallic inserts considerably reduces the effect of corrosion on the measured tensile-shear force of corroded assembly compared to non-corroded assembly. However, it affects the force-displacement response and failure mode compared to the response of aluminium-stainless steel assembly without bimetallic insert due to its effects on the bolt rotation and stress distribution. This needs to be considered in the design of dissimilar material bolted assembly.

Introduction

The improved corrosion resistance of aluminium and stainless steel promotes their use in seawater environment to increase the durability of maritime structures. Aluminium offers weight savings at the cost of strength, while stainless steel offers superior strength at the cost of added weight (Gupta et al., 2020; Lundberg, 2016). The optimal user-scenario is to combine aluminium and stainless steel in a multi-material structure. This however involves serious challenges related to the components joining (Shifler, 2005; Martinsen et al., 2015; Montemor, 2016). A major concern when combining stainless steel and

aluminium components in marine environment is the degradation of aluminium components due to galvanic corrosion. The galvanic corrosion is an electrochemical process in which one less noble material corrodes preferentially when it is in electrical contact with more noble material in the presence of an electrolyte (Shifler, 2005; Martinsen et al., 2015; Montemor, 2016; Vargel, 2004; Zhang et al., 2019; Suo et al., 2021). For the system discussed herein, aluminium is less noble than stainless steel and may suffer from corrosion in an aqueous environment. The aluminium in the assembly act as a sacrificial anode and corrodes faster depending on several environmental factors such as alloy metal-lurgy and chemistry, water chemistry, potential of hydrogen pH,

* Corresponding author.

E-mail address: afaf.saai@sintef.no (A. Saai).

<https://doi.org/10.1016/j.jajp.2023.100163>

Available online 8 November 2023

2666-3309/© 2023 The Author(s). Published by Elsevier B.V. This is an open access article under the CC BY license (<http://creativecommons.org/licenses/by/4.0/>).

pollution and contamination, geometry, surface roughness, and temperature (Shifler, 2005; Martinsen et al., 2015; Montemor, 2016).

Research and development efforts were devoted to defining standards or methods to reduce the effects of galvanic corrosion on the integrity of multi-material structures (Langøy, 2023; EN 1090-3, 2019; NORSOK Standard - M-102, 2015; NORSOK Standard – M-001: 2014/A1, 2021). For example, EN 1090-3 (EN 1090-3, 2019) and NORSOK M-001 (NORSOK Standard – M-001: 2014/A1, 2021) specifies that when joining dissimilar materials such as aluminium and steel, the aluminium surfaces shall be treated (e.g., coating) or the different metals shall be separated by an isolation to avoid galvanic corrosion (Suo et al., 2021; Melhem, 2019; Jun et al., 2021). In the case of high load applications where non-metallic isolation can't be applied, the standard recommends bimetallic shim or insert as an alternative solution (NORSOK Standard - M-102, 2015). To the best of our knowledge, there is a lack of scientific studies on the applicability of such bimetallic inserts and their impacts on corrosive and mechanical response of aluminium and stainless steel bolted connections. Therefore, the effects of bimetallic insert on corrosion, material degradation, loading capacity, stress distribution, strain distribution and failure of aluminium – stainless lap shear bolted connection were investigated by the mean of experimental tests and numerical modelling. The single bolt lap shear assemblies of aluminium and stainless steel plates were performed in two settings. In one of them a bimetallic insert was applied in accordance with the current recommendation to avoid galvanic corrosion (NORSOK Standard – M-001: 2014/A1, 2021). Considering that the aluminium plays the role of sacrificial anode in the aluminium – stainless steel galvanic couple, a single bolt lap shear assembly joining two aluminium plates is also considered as a reference assembly for the evaluation of aluminium – stainless steel bolted assemblies. A stainless steel bolts with the quality required by the standards (NORSOK Standard – M-001: 2014/A1, 2021) were used in all assemblies. The effect of the bimetallic insert on the load capacity, fracture mode, stress distribution and strain distribution were determined by tensile-shear testing method (ISO 12996, 2013) for three different conditions: dry condition, six week of accelerated corrosion test, and at 16 week of accelerated corrosion test. Fig. 1 shows an overview of the assemblies and testing conditions.

Tensile-shear test is commonly used to assess the static bearing force and failure mode of bolted assembly (Li et al., 2021; Kong et al., 2021; Denkert et al., 2022; Boretzki and Albiez, 2023; Delzendehtrooy et al., 2022; Kong et al., 2021). In the current work, the testing setup is equipped with three optical cameras and digital image correlation (DIC) software to provide full-field measurements of plates displacements and bolt's rotation. The full-field measurements of displacements were demonstrated as a reliable tool for analysing strain localization and failure modes (Delzendehtrooy et al., 2022; Haris et al., 2017; Sozen and Guler, 2011). They will be used to study the effects of bimetallic insert on the force and strain distribution in dry and corrosive conditions (see Fig. 1). The corrosion conditions tested were obtained by accelerated corrosion testing method. Accelerated corrosion tests are widely used to simulate a corrosive environment by laboratory testing methods

(Meikle et al., 2017; Calabrese et al., 2015; Del Real et al., 2006; Mariam et al., 2017). Standard method such as ISO 9227:2012 (ISO 9227, 2012) is usually used to specify the apparatus, the reagents, and the method employed to evaluate the corrosivity of the simulated environment. Other standards for modified salt spray testing, such as ASTM B117 (ASTM B 117, 2018) and ASTM G8 (ASTM G85, 2019), involve more aggressive test conditions like using a test solution with a lower pH, by alternating corrosive and neutral atmosphere or by using an aggressive electrolyte mix for more corrosion resistant materials. Testing methods such as ASTM G116 and ASTM G104 (ASTM G 116, 1999; ASTM G104, 1989) describes laboratory testing methods for the evaluation of atmospheric galvanic corrosion. In this work, a cyclic salt spray corrosion test method (ISO 11997-1, 2017) was considered. The spray solution was prepared by dissolving sodium chloride (NaCl) in water to give a concentration of 50 g/l. The main measurements from the corrosion tests are the corrosion rate (weight loss) and the surface degradation, e.g., the size and the depth of corrosion attack. They were determined for the assemblies and conditions presented in Fig. 1.

The effects of bimetallic insert were analysed by a comparative study of the measurements of tensile-shear tests and accelerated corrosion tests for the investigated assemblies and conditions. A critical challenge to the assessment of corrosion's effect on loading capacity lies in the assessment of the effects on preloading and frictional behaviour. Tribocorrosion studies on materials like aluminium and stainless steel demonstrated an increase in their friction coefficient due to corrosion, affecting contact shear forces (Zhang et al., 2015; Li et al., 2021; Zhang et al., 2018). Material degradation due to corrosion cause reduction in the preloading and degradations of mechanical performance (Kong et al., 2021; Kong et al., 2022; Jiang et al., 2022; Kim et al., 2016; Li et al., 2021). At the same time, it is known that the corrosion products built up under the washer, nuts and bolt head increase the clamping force leading to serious issue for the design of bolted assembly (Bickford, 1995). The formation of corrosion products is critical issue facing the design of bolted assembly due to their effects on preload and frictional force.

To support the understanding of the effects of preload and friction on the response of lap shear bolted assemblies, finite element simulations were performed with varying preloads and friction coefficients. Elastoplastic material models with ductile damage criterion were used to mimic the mechanical response of aluminium and stainless steel plates. The material models were calibrated using tensile measurements performed on specimens prepared from aluminium and stainless steel plates. The assembly model was evaluated based on the experimental measurements of tensile-shear test in dry conditions. Preliminary analysis of the effects of preload and friction are discussed versus experimental measurements from tensile-shear tests on non-corroded and corroded bolted assemblies.

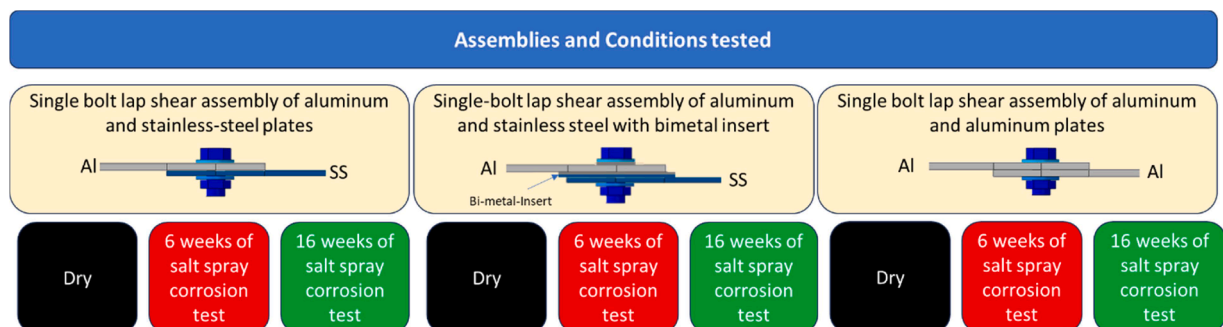


Fig. 1. Overview of bolted assemblies and testing conditions.

Materials and experiments

Materials

Aluminium alloy AA6082 and stainless steel 316 L were selected as representative materials of marine grades which can be used for structural applications in corrosive environment. Both materials have improved mechanical strength and corrosion resistance. Aluminium alloy 6082 has the highest strength to weight ratio among the 6XXXX series due to the addition of a larger amount of manganese which enable to control the grain structure. This makes it an attractive choice as a structural aluminium alloy. The stainless steel 316 L grade is a low carbon austenitic stainless steel where the addition of molybdenum and reduced amount of carbon give an improved corrosion resistance. The AA6082 was supplied in the form of extruded plate with thickness $t_{Al} = 3.7 \text{ mm}$. The stainless steel 316 L was supplied in the form of laminated plate (ASTMA240M/A4B0M-09) with thickness $t_{SS} = 3 \text{ mm}$. The material composition of the aluminium and the stainless steel plates are given in Table 1. The bolting system consists of a fully threaded hexagon-head bolt $M10 \times 20$ made of stainless steel A4 (DIN 933), nut $M10$ made of stainless steel A4 (DIN 934), two washers ($\varnothing 10.5$) made of stainless steel A4 (DIN 125) and one aluminium washer $\varnothing 10.5 \text{ mm}$ with 2 mm thickness machined from the AA6082 plate. The aluminium washer is only used in the aluminium – stainless steel assembly with the bimetallic insert.

Single bolted assemblies

Fig. 2 illustrates the different settings of single bolted assemblies investigated in this study, which will be referred to by:

- "Al-SS" for single bolt lap shear assembly joining aluminium plate and stainless steel plate without bimetallic insert, using a stainless steel bolt, a stainless steel nut, and two stainless steel washers,
- "Al-SS-Bi" for single bolt lap shear assembly joining aluminium plate and stainless steel plate, using aluminium-stainless steel bimetallic insert placed between the two plates and aluminium-stainless steel bimetallic washer placed between the aluminium plate and the bolt head. A stainless steel bolt is used with stainless steel nut in the contact with stainless steel plate.
- "Al-Al" for single bolt lap shear assembly joining two aluminium plates using a stainless steel bolt, a stainless steel nut, and two stainless steel washers.

The geometry of the plates, inserts, bolts, and washers in the assemblies are illustrated in Fig. 2. The geometry of bimetallic insert was defined according to standard practice (NORSK Standard – M-001: 2014/A1, 2021) which specify that the geometry of the insert should be larger than the plate to prevent galvanic corrosion due to water wetting of aluminium and steel. The same tightening torque was carefully applied on all assemblies. A torque wrench with a measurement's precision equals to $\pm 4 \%$ was used to apply an identical tightening torque of $T = 69 \text{ N.m}$. The aluminium and stainless steel plates in all assemblies have the same in-plane dimensions (200 mm length \times 50 mm width).

Table 1

Alloying elements of aluminium AA6082 and stainless steel 316 L plates given in %weight.

Aluminium alloy AA6082								
Si	Mg	Fe	Cu	Mn	Cr	Ti		
1.01	0.80	0.19	0.06	0.54	0.15	0.02		
Stainless steel 316L								
C	Si	Mn	P	S	Ni	Cr	Mo	N
0.017	0.49	1.80	0.033	0.001	10.1	17.10	2.07	0.043

The thicknesses of the aluminium plates and the stainless steel plates in all assemblies are 3.7 mm and 3 mm , respectively. The assembly plates were machined from the supplied aluminium extruded profile and the stainless steel sheet in a way that the tensile direction is aligned with the extrusion direction and rolling direction respectively. All plates were cleaned with acetone before assembling to remove any residuals from machining. For all assemblies, the overlap of the assembled plates is 50 mm .

The bimetallic inserts in the assembly Al-SS-Bi were obtained by gluing two small plates ($60 \times 55 \times 2 \text{ mm}^3$) machined from a AISI316L laminated plate and a AA6082 extruded profile. The glue is fast-acting epoxy resin adhesive (ESK-50) from WÜRTH. The aluminium washer is added below the stainless steel washer under the bolt head. The aluminium and stainless steel washers were glued using the same epoxy resin adhesive.

Material testing for model calibration

The stress-strain curves required for the calibration of material models were obtained by standard tensile tests performed on the materials specimens extracted from AISI316L laminated plate and AA6082 extruded profile. The geometry of tensile specimens is illustrated in Fig. 3. The tensile directions were aligned with the extrusion direction of AA6082 extruded profile or rolling direction of the AISI316L laminated plate. The tensile tests were performed at room temperature and quasi-static strain rate using an Instron tensile machine with a loadcell of 250 kN . The displacement rate was set to 9 mm/min . The digital image correlation (DIC) was used to measure the displacement from which the tensile strains were calculated using a reference gauge length of 55 mm . The engineering stress–strain curves for the aluminium and stainless steel plates are plotted in Fig. 3 and show good repeatability.

The bolts, nuts and washers were supplied according to standard requirements. Their mechanical properties were assumed to be equal to the standard properties of austenitic stainless steel A4-80 grade in accordance with ISO 3506-1:1997, i.e., yield stress $R_{p 0.2} = 600 \text{ MPa}$, ultimate tensile strength $R_m = 800 \text{ MPa}$ and elongation at fracture $A = 30 \%$.

Assemblies testing

Fig. 4 shows the chronological arrangement of cyclic salt spray corrosion (CSSC) tests, tensile-shear tests, and corrosion characterizations with the number of specimens used for each assembly and for each test. The assemblies testing involves a total number of 39 joint specimens divided in three groups, each of them has 13 specimens which are representative of one type of the assemblies illustrated in Fig. 2. As illustrated in Fig. 4, the tensile-shear tests were performed on 3 joint specimens from each assembly at the reference condition (non-corroded), while the remaining specimens (10 specimens for each assembly) were prepared for CSSC testing. After six weeks of CSSC testing, five specimens from each assembly were collected for mechanical testing and corrosion characterization. From the collected specimens for each assembly, three specimens were used for tensile-shear testing while the two other specimens were disassembled to perform corrosion characterizations. The remaining 15 specimens (5 for each assembly type) continued CSSC testing during additional 10 weeks. They were collected after a total 16 weeks of CSSC testing, when three specimens from each assembly were used for tensile-shear tests, and two specimens were disassembled for corrosion characterizations.

The specimens for corrosion characterization were cleaned in accordance with the following procedure. The loose corrosion products were first removed in running tap water by light brushing with a non-metallic bristle. Then they were rinsed in distilled water before chemical cleaning in concentrated nitric acid for about 10 min. Finally, they were rinsed in distilled water and dried.

The tensile-shear tests were performed at ambient temperature

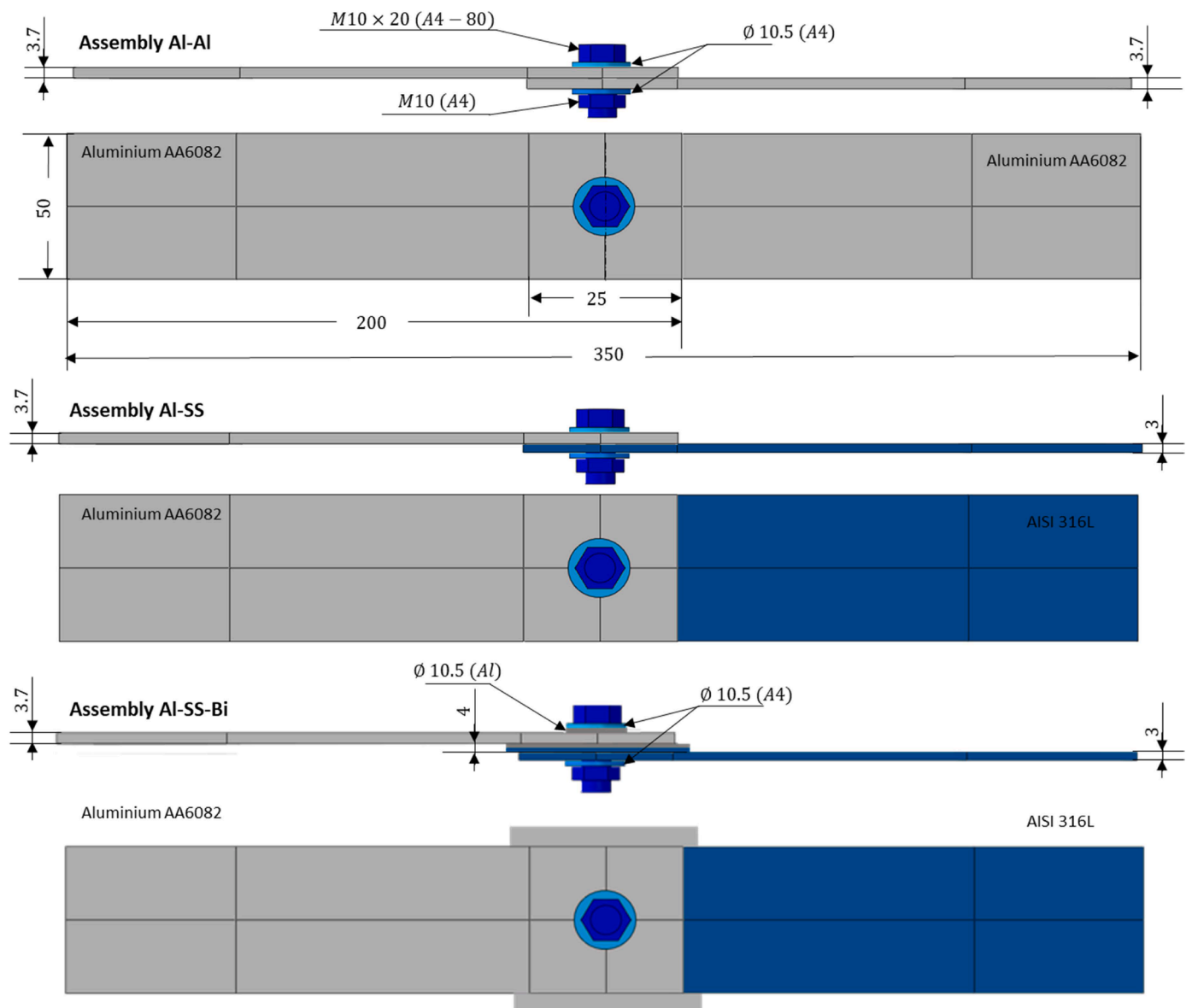


Fig. 2. Schematic illustration showing the three assemblies for tensile-shear and corrosion tests.

directly after the salt spray corrosion tests. Since the tensile-shear test has a short duration, the humidity of the tensile testing machine environment is assumed to not affect the testing results. The main measurements of the tensile-shear test are the force determined by the load cells of the tensile machine and the displacement/rotation determined by the DIC acquisition system, which are synchronized during the test. The crosshead motion was set to enable a quasi-static displacement rate ($< 9 \text{ mm/min}$) with high frequency (4.5 Hz) of image acquisition for the DIC system. Since the DIC is acting as a digital extensometer directly placed on the tested specimen, it provides local measurements with higher precision compared to the crosshead measurement. A DIC virtual extensometer with reference gauge length of 120 mm (see Fig. 5) was used in all assembly to determine the displacement.

The visible surfaces of the joint specimens for tensile-shear testing were thinly coated with white paint and sprayed with black paint to obtain random patterns (see Fig. 5). Such patterns are required for DIC analysis. Two shim plates were used for clamping each joint specimens in the grips of the tensile machine to ensure force concentricity. The thickness of the shim plate in each holder equals to the thickness of the assembly plate in the opposite holder. The top plate and bottom plate

during tensile-shear tests were observed by two cameras oriented perpendicularly to the plates. A third camera was placed on the joint side to access the rotation of the bolt. The acquisition system recorded images at a 4.5 Hz frequency with an average resolution of 900×2980 for the cameras shooting the plates and 650×2980 pixels for the side camera. The acquisitions system of the three cameras were synchronized with the tensile machine data acquisitions. All recorded images were post processed using the eCorr software (DIC Software, 2017). A virtual grid was associated to the initial image, with a grid step of 15 pixels and a pattern size of 15 pixels. The DIC analysis was performed to determine the full-field displacements of the observed plates. A virtual extensometer with 120 mm length was defined in a way that the centre of the extensometer coincides with the centre of the bolt to determine the tensile-shear displacement in a similar manner for all assemblies (see Fig. 5). Another virtual extensometer was aligned with the bolt axis in the image from the side camera to determine the bolt rotation.

The cyclic salt spray corrosion tests were performed in Ascot-Cyclic testing cabinet. The spray solution was prepared by dissolving sodium chloride (NaCl) in water to give a concentration of $50 \pm 5 \text{ g/L}$. The pH of the sprayed solution was adjusted to 8.2 at $25 \pm 2 \text{ }^\circ\text{C}$. The salt fog

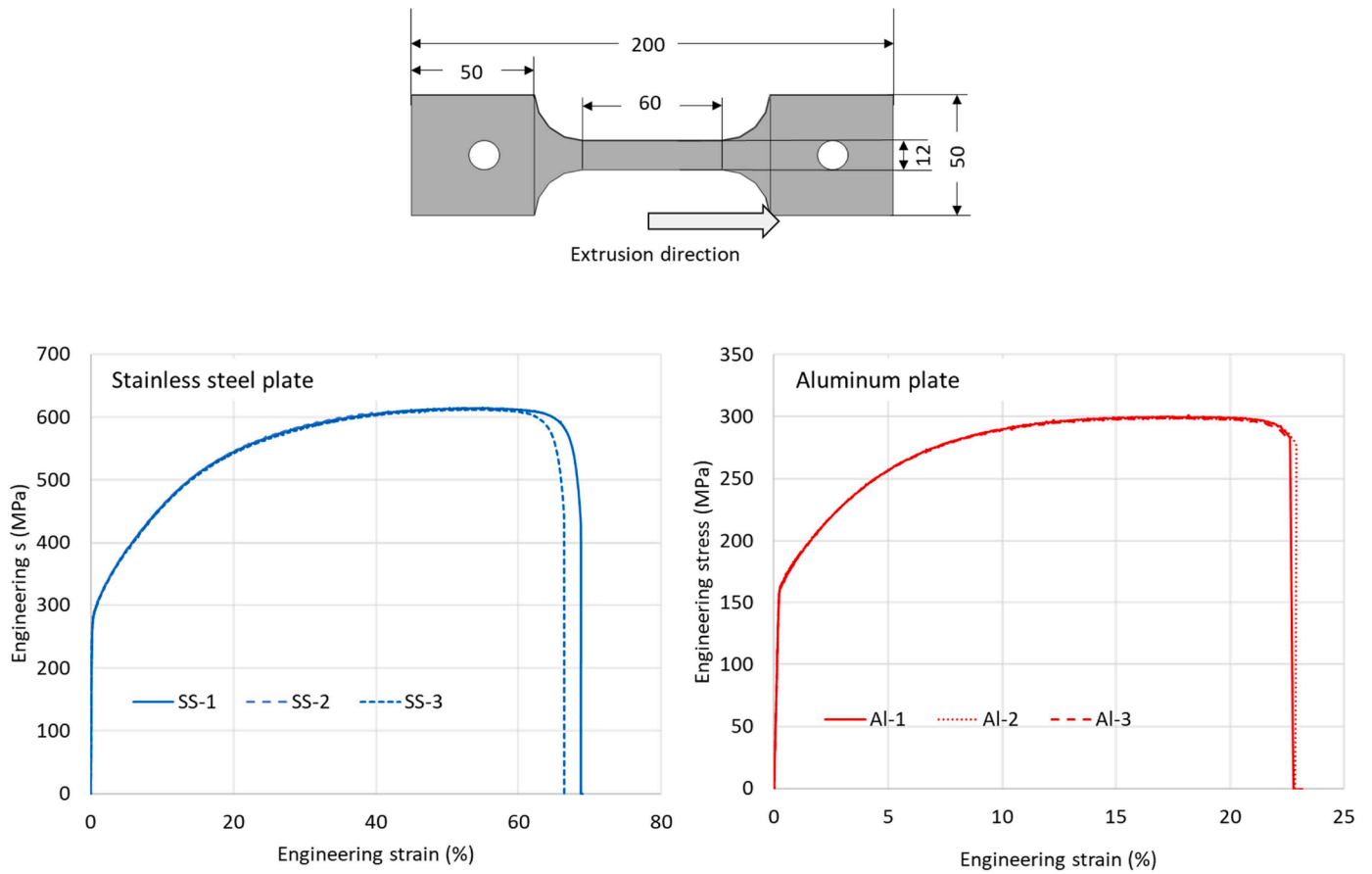


Fig. 3. Engineering stress- strain curves of AA6082 (right-side) and stainless steel 316 L (left-side). Specimen’s geometry is on the upper part of the figure with dimensions in mm.

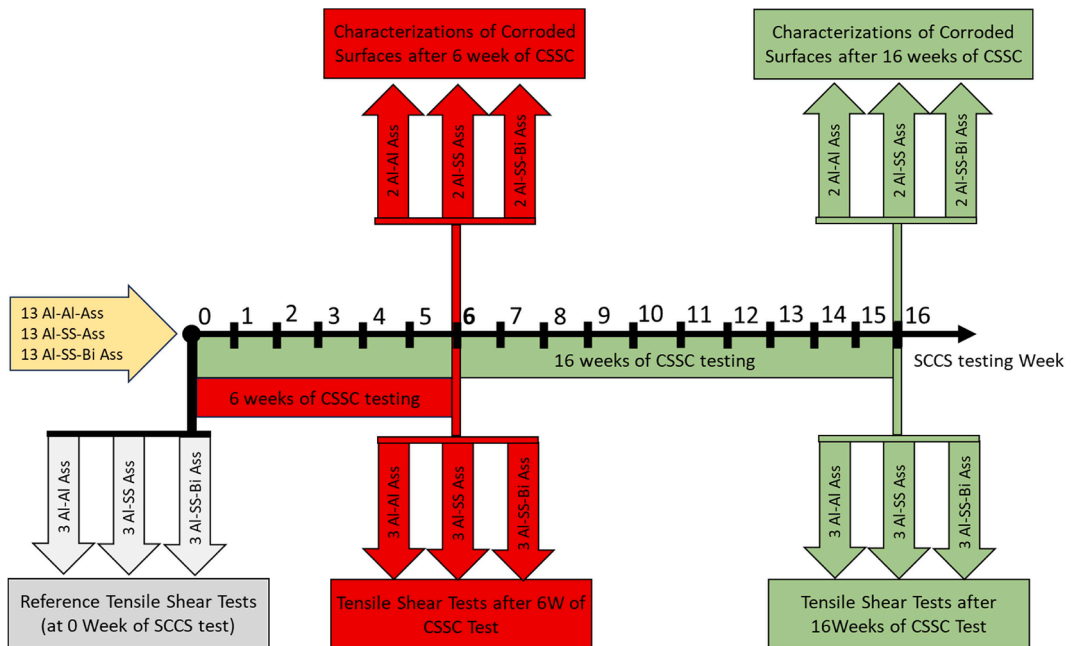


Fig. 4. Timeline showing the chronological arrangement of tensile-shear tests, cyclic salt spray corrosion (CSSC) tests and corrosion characterizations with the number of specimens used for each test.

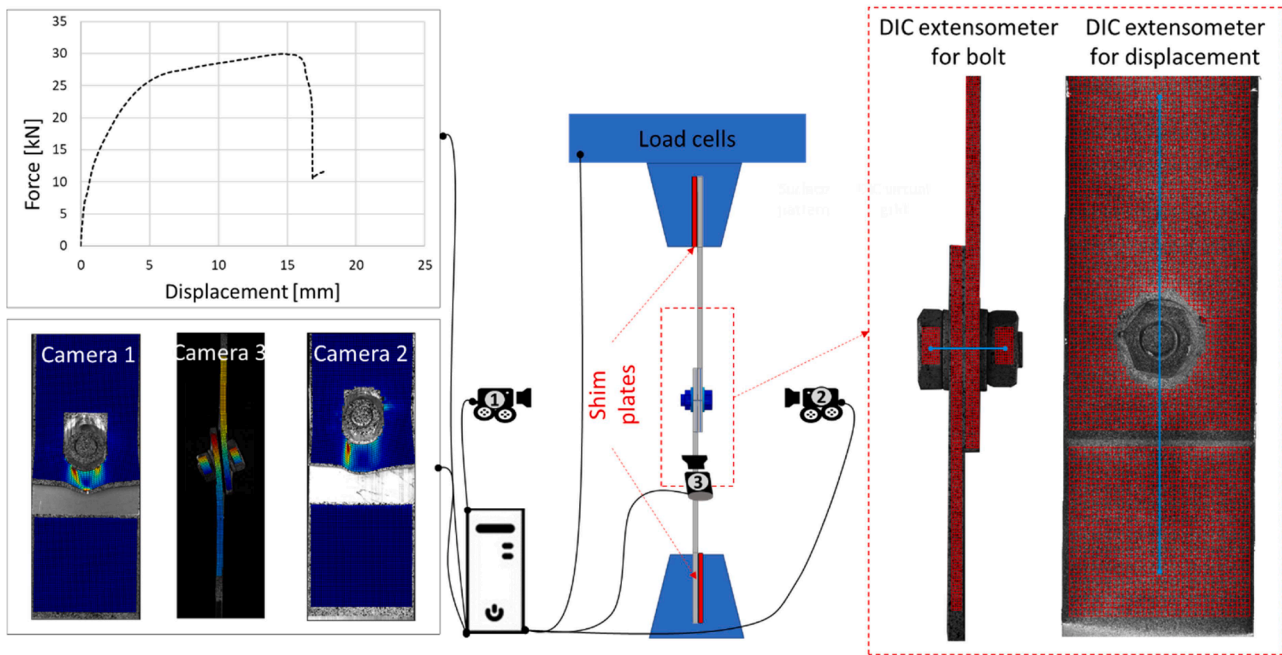


Fig. 5. Setup of tensile-shear test showing test arrangement with shim plates (in red) and three cameras to assess the deformation of both plates and the rotation of the bolt. The measurements of tensile machine and digital image correlation (DIC) are synchronized.

Table 2

Specification of cyclic salt spray corrosion test.

Step	Condition	Period	Temperature
Step 1	Salt spray	2 h	35 ± 2
Step 2	Dry with 20 % – 30 % RH	4 h	50 ± 2
Step 3	Wet with 95 % RH or over	2 h	50 ± 2

deposition was 1 – 2 ml/h determined for fog collected over periods of 24 h. The CCT cabinet was prepared to perform three-steps cycles with a total time of 8 h from step 1 to step 3 as specified in Table 2. The transition time to reach the temperature and relative humidity specified for a condition is within the standard requirements (ISO 11997-1, 2017).

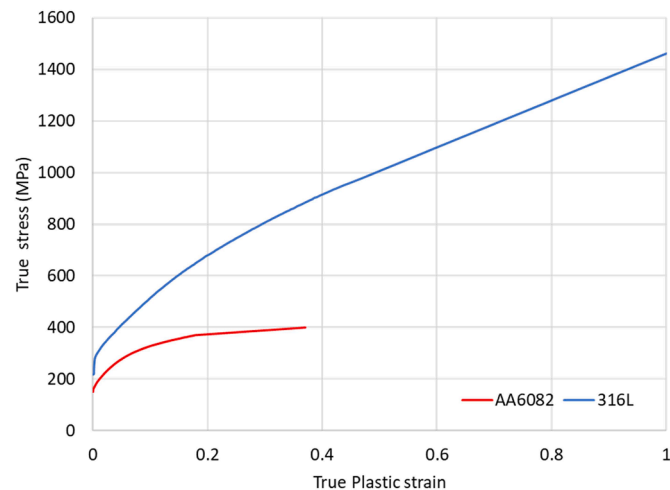


Fig. 6. Elastoplastic material models of aluminium AA6082 and stainless steel 316 L, utilized in the FE simulations using tabular inputs.

Numerical modelling

Material modelling and calibration

Both aluminium and stainless steel were assumed to be homogeneous and isotropic materials. Their response was simulated using elastoplastic model calibrated based on the true stress-strain curves determined by tensile tests (Fig. 6). The material hardening was introduced as tabular inputs in the FE simulations and the von Mises yield criterion was considered. The damages responses were predicted using uncoupled damage model. The damage accumulation is assumed to not affect material plasticity and is described using a weighting function (Hu et al., 2018; Lou et al., 2012; Pater et al., 2020; Talebi-Ghadikolaee et al., 2020). The damage initiation is described based on the normalized Cockroft–Latham ductile fracture criteria (Pater et al., 2020; Talebi-Ghadikolaee et al., 2020):

$$d^f = \int_0^{\epsilon_p^f} \left(\frac{\sigma_{max}}{\sigma} \right) d\epsilon_p \tag{1}$$

where D^f is the critical damage parameter, ϵ_p is the equivalent plastic strain, σ_{max} is the maximum principle stress and σ is the equivalent stress. The maximum stress and equivalent stress are related to stress triaxiality (η) and normalized Lode angle parameter ($\bar{\theta}$) (Talebi-Ghadikolaee et al., 2020; Bai and Wierzbicki, 2010):

$$\eta = \frac{\sigma_m}{\bar{\sigma}} \tag{2}$$

$$\sigma_{max} = \bar{\sigma} \left(1 + \frac{2\cos\left(\frac{\pi}{6}(1-\bar{\theta})\right)}{3\eta} \right)$$

By neglecting the lode, a simplified expression of the effective fracture strain can be obtained from the integration of Eq. (1) with consideration of Eqs. (2) and (3):

$$\epsilon_p^f = \frac{d^f}{\eta + \left(\frac{2}{3} \cos\left(\frac{\pi}{6}\right)\right)} \quad (3)$$

The effective fracture strains were determined by DIC for aluminium plate ($\epsilon_p^f = 0.23$) and stainless steel plate ($\epsilon_p^f = 1.01$) and correspond to a stress triaxiality of $\eta = 0.33$. They were used to calibrate the critical damage parameter for aluminium ($d_{Al}^f = 0.22$) and stainless steel ($d_{SS}^f = 0.99$). Then, the calibrated parameters were used to compute the effective fracture strains as a function of stress triaxialities using Eq. (3) (see Fig. 7). The damage evolution after damage initiation is assumed to represent progressive degradation of the material stiffness. The softening response after damage initiation is described by a stress-displacement response, introducing the equivalent plastic displacement as the fracture work conjugate of the yield stress after damage initiation (Hillerborg et al., 1976). The stress degradation in an element is described by $\sigma = (1 - D) \bar{\sigma}$, where σ and $\bar{\sigma}$ are respectively the stress after damage initiation and the stress computed in the absence of damage. The damage variable D is described by a power law as a function of the equivalent plastic displacement (U_p):

$$D = \left(\frac{U_p}{U_p^f}\right)^n \quad (4)$$

where n is the power law exponent and U_p^f is the equivalent plastic displacement at failure. The value of U_p^f vary depending on the characteristic length of the finite element mesh. The values of n and U_p^f were determined for element characteristic length of 1 mm by inverse identification based on the tensile test measurements. The values of U_p^f and n for aluminium plate are respectively 0.19 mm and 2 . The values of U_p^f and n for stainless steel plate are respectively 0.2 mm and 24 . The values of U_p^f are valid for finite element simulations with mesh having characteristic length of 1 mm . Therefore, structural mesh was used in all FE simulations to ensure equivalent mesh with few elements having very small deviations from the characteristic length of 1 mm . Fig. 7 shows the effective fracture strain and the damage variable as computed by Eqs. (3) and (4) respectively. As can be observed, the high values of n leads to a slow degradation process of the material stiffness right after damage initiation; and then the degradation accelerates shortly before failure.

The engineering stress-strain curves predicted by FE simulations are compared to experimental measurements of tensile tests in Fig. 9. The calibration of the material model based on the tensile test results explains the good agreement between FE simulations and experimental

measurements in Fig. 8. However, it must be mentioned that aluminium deformations are anisotropic and involve complex mechanisms, where the mechanical response depends on the combined effects of microstructure and loading path (Saai et al., 2013; Saai et al., 2011a; Saai et al., 2011b). The simplified model and calibration process of aluminium based on tensile test might affect the prediction accuracy of aluminium model in complex load scenario and state of stress. Advanced material model and calibration process based on shear and biaxial test will improve the model prediction.

The bolt, nut and washers were considered to have elastoplastic behaviour with linear hardening plastic responses. Since no tests were performed on the bolt and the washers, the minimal required properties of austenitic stainless steel A4-80 grade according to ISO 3506-1: 1997 were used to build the material model : A young modulus of $E = 210\text{ GPa}$, a yield stress of $\sigma_y = R_{p\ 0.2} = 600\text{ MPa}$, a fracture elongation of $A = 30\%$ (Giving a true strain of $\epsilon_f = \ln(1 + A) = 0.26$) and an ultimate strength of $R_m = 800\text{ MPa}$ (Giving a true stress of $\sigma_f = R_m(1 + A) = 1040\text{ MPa}$ assuming an incompressible plastic flow). The slope C of the linear plastic hardening curve for the bolt, nut and washers was thus determined using the equation:

$$C = \frac{\sigma_f - \sigma_y}{\epsilon_f - \frac{\sigma_y}{E}} \quad (5)$$

leading to $\sigma = C\epsilon_p + \sigma_y$, if $0 < \epsilon_p < \epsilon_f - \frac{\sigma_y}{E}$, where ϵ_p is the plastic strain.

Assembly modelling

The FE simulations of the tensile-shear tests of the investigated lap shear bolted assemblies were performed using ABAQUS explicit analysis solver. Each simulation was divided into two stages (Fig. 11). The first stage simulates the preload associated with the bolt tightening and the second stage simulates the tensile-shear load of the assembly. Fig. 10 shows the size and the distribution of the mesh element in the assembly. As required by the damage model, a characteristic length of 1 mm was considered for the elements in the plates in all assemblies. Solid brick elements with reduced integration were used in the finite element mesh. A simplified representation of the bolt and the nut were considered assuming non-threaded contact surfaces. The contact surfaces between the bolt and the holes of the plates are also assumed to be non-threaded.

All surface contacts are assumed to have tangential frictional behaviour and normal hard contact to avoid the penetration of the contacting surfaces under pressure. The frictional behaviour is described by penalty formulation using friction coefficient. The reference value of friction coefficients for aluminium – aluminium surface pairs is

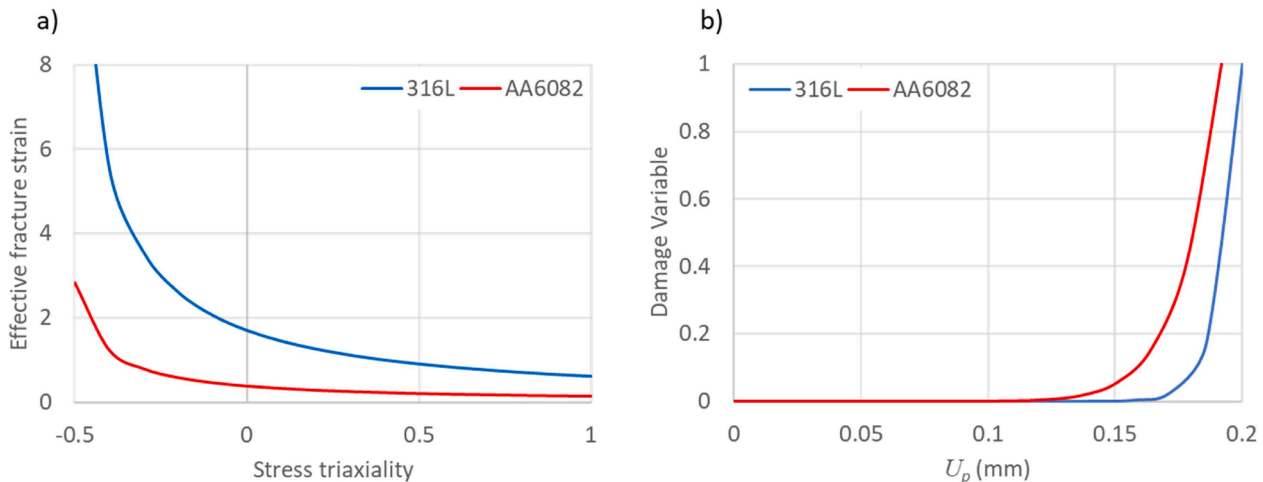


Fig. 7. a) Effective fracture strain computed by Eq.(3) as a function of stress triaxiality and b) Damage variable computed by Eq.(4) as a function of equivalent plastic displacement after damage initiation for AA6082 and 316 L.

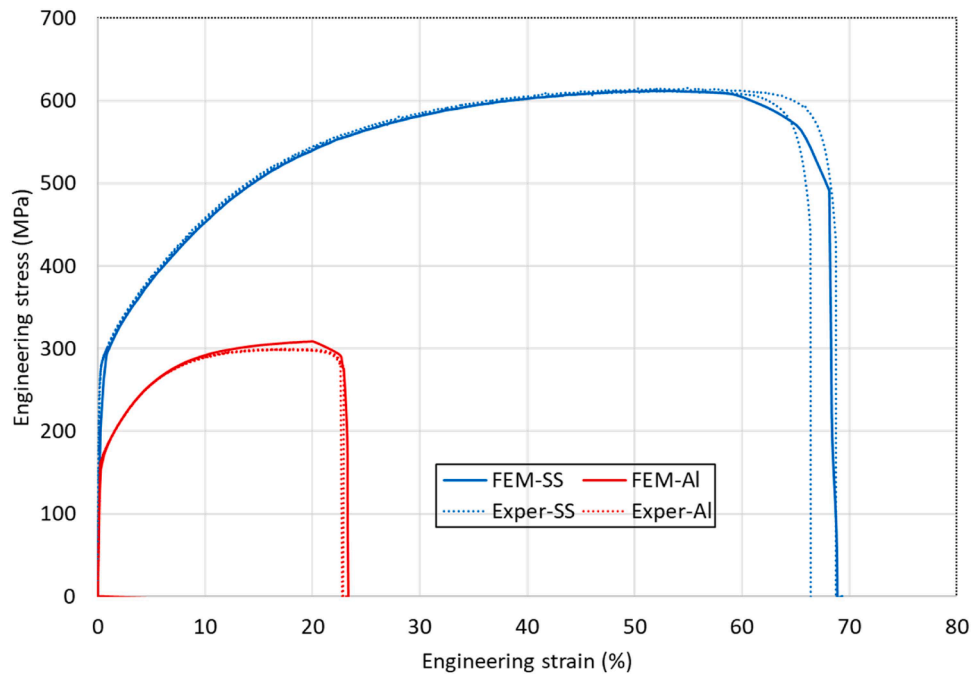


Fig. 8. Engineering stress- strain curves determined by FE simulations compared to experimental measurements.

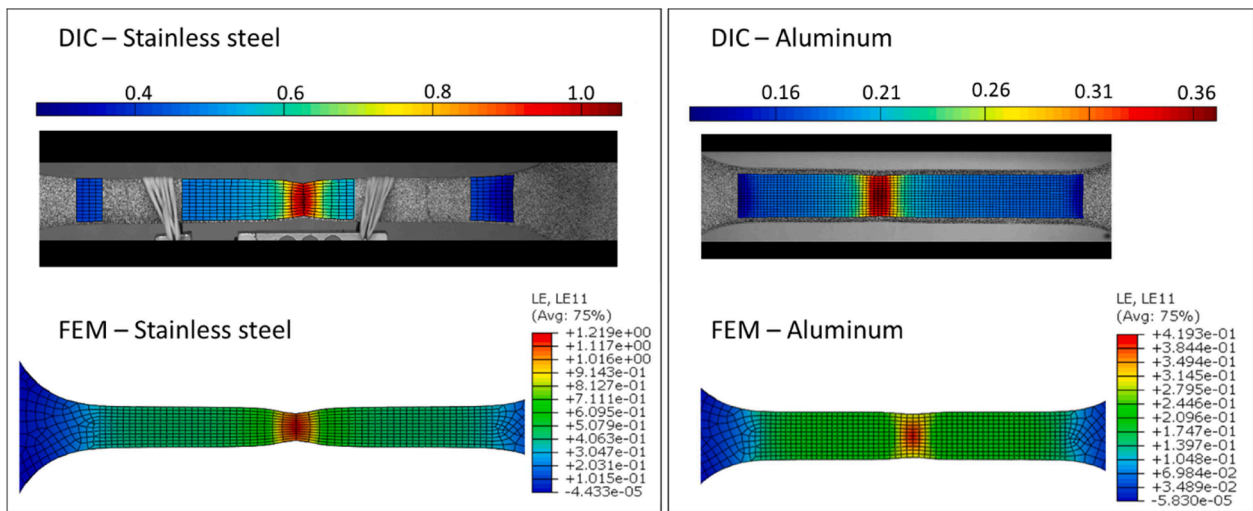


Fig. 9. Tensile strain at fracture as determined by the FE simulations compared to DIC measurements.

$\mu_{Al-Al} = 0.2$ for aluminium - stainless steel surface pairs is $\mu_{Al-SS} = 0.14$, and for stainless steel surface pairs $\mu_{Al-SS} = 0.1$. The effects of corrosion on the preload and frictional response were investigated by numerical simulations by varying the preload and friction (ref. Section 4.2.2).

The preload in step 1 was calculated using the following simplified relation between the clamping force (F_n) and the preload torque:

$$F_n = \left(\frac{T}{k d} \right), \tag{6}$$

where, T is the tightening torque, d is nominal diameter of the nut and k is a factor depending on the friction. Considering the reference torque $T = 69.8 \text{ N.m}$ and $k = 0.3$ for non-lubricated assembly the reference clamping force $F_n = 23 \text{ kN}$ were applied in all assemblies to simulate the preloading of the bolts. In the step 2 simulating the tensile-shear load, a tie contact is applied between the nut and the bolt. To simulate tensile shear load, the displacements of the nodes in the grip area of one of the

plates in the assembly were constrained in all directions, while the displacements of the nodes in the grip area of the other plate were given a constant velocity in the tensile-shear direction and constrained in the other two directions (see Fig. 11).

Comparative study

In this section, the experimental observations and measurements of the different assemblies are presented and discussed to evaluate the effects of bimetallic inserts on corrosion and mechanical performance of aluminium-stainless steel bolted assembly as well as the effects of galvanic corrosion on the tensile-shear force and failure modes. Then, the FE simulation results are presented and discussed to evaluate the effects of the changes in preloading and frictional response due to the formation of corrosion products.

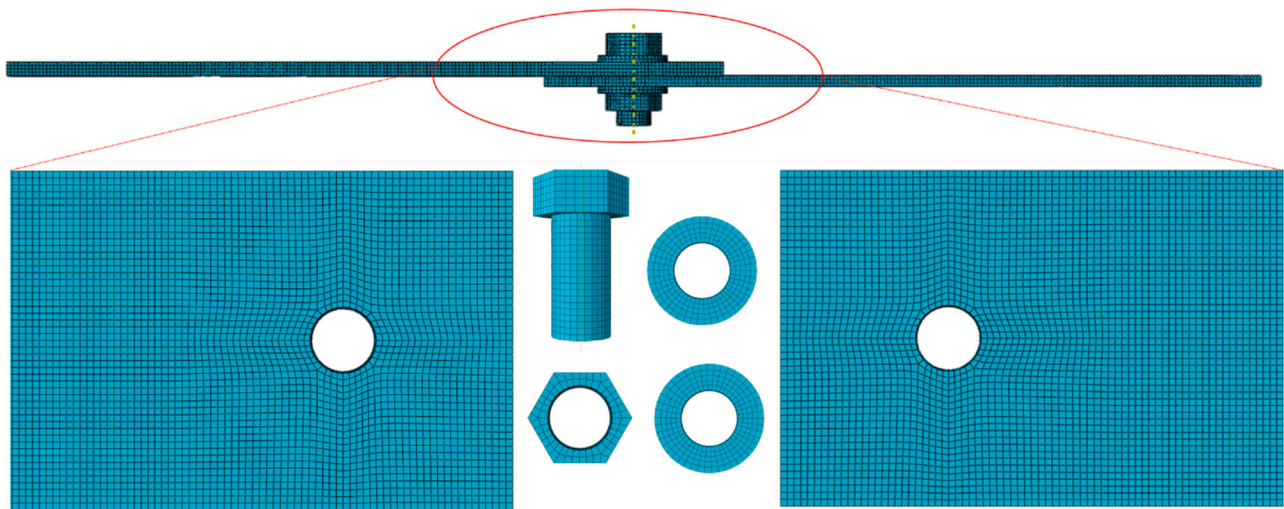


Fig. 10. FE representation of the connection elements showing the mesh details.

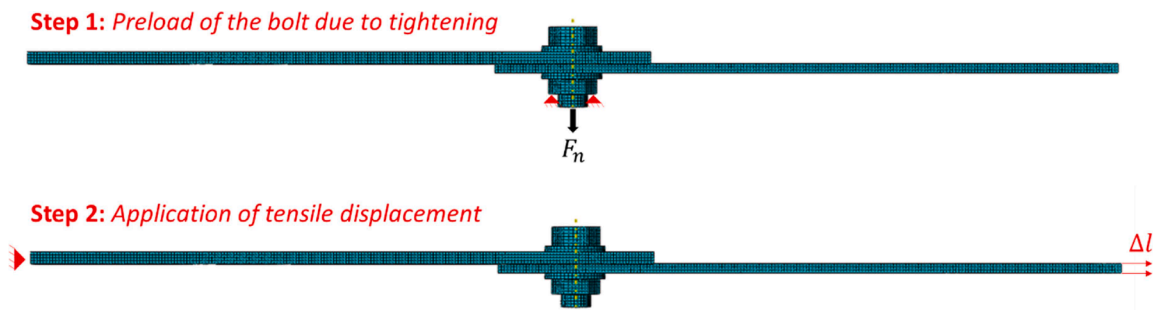


Fig. 11. Schematic illustration of the conditions applied on the bolt and nut during tightening and tensile-shear testing.

Table 3

Overview of corrosion measurements for the aluminium plates with deviation computed by s/\sqrt{n} , where s is the standard deviation and n is the number of tests.

	6 Weeks of CSSC			16 Weeks of CSSC		
	Average weight loss per plate (g)	Average depth (μm)	Maximum depth (μm)	Average weight loss per plate (g)	Average depth (μm)	Maximum depth (μm)
Al-Al	0.02 ± 0.003	234 ± 14	374 ± 32	0.027 ± 0.003	379 ± 25	656 ± 49
Al-SS	0.08 ± 0.004	290 ± 27	448 ± 35	0.15 ± 0.05	505 ± 40	632 ± 1
Al-SS-Bi	—	111 ± 7	210 ± 35	—	276 ± 37	457 ± 24

Experimental observations

Corrosion measurements

Due to the galvanic difference between aluminium and stainless steel, the corrosion takes place in aluminium plates. Therefore, the corrosion measurements of weight loss are associated with the aluminium plates. Table 3 overviews the measurements of the weight loss and the depth of corrosion attack. Note that the aluminium - stainless steel assembly with bimetallic inserts includes epoxy resin adhesive, which was removed during the cleaning process. This presents a source of inaccuracy in the weight loss measurement of Al-SS-Bi assembly. Thus, the weight loss of Al-SS-Bi assembly were omitted in Table 3 and only the depth of corrosion attack was presented and compared to the corresponding measurements of Al-Al and Al-SS

assemblies.

Fig. 12 shows that connecting the aluminium plate to the stainless steel plate in Al-SS assembly accelerates the corrosion process and increases the weight loss by a factor of 4–5 due to the galvanic difference between the aluminium and the stainless steel. The aluminium plate is acting as a sacrificial alloy in this assembly. As illustrated in Fig. 12-a, the aluminium may act passive and suffer from local corrosion or be active and suffer from uniform corrosion. Most commercial aluminium alloys act passive in the pH mid-region 4–9 but become electrochemically active at high and low pH. For the test environment applied in the experiments presented herein, the pH was adjusted to 8.2, i.e., the aluminium will form a passive surface (Al_2O_3). However, passive surfaces are susceptible to local corrosion like, e.g., crevice corrosion and pitting corrosion, especially in the presence of chloride ions, unless they

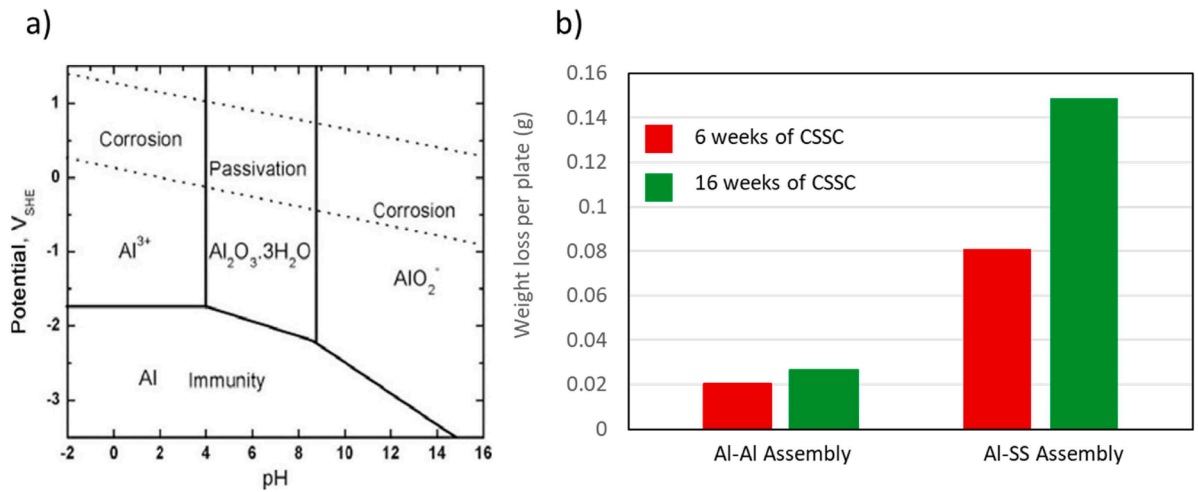


Fig. 12. a) Pourbaix diagram of aluminium (Pourbaix, 1966) and b) Average aluminium weight loss per plate for Al-Al assembly and Al-SS assembly without inserts after 6 weeks (red) and 16 weeks (green) of CSSC testing.

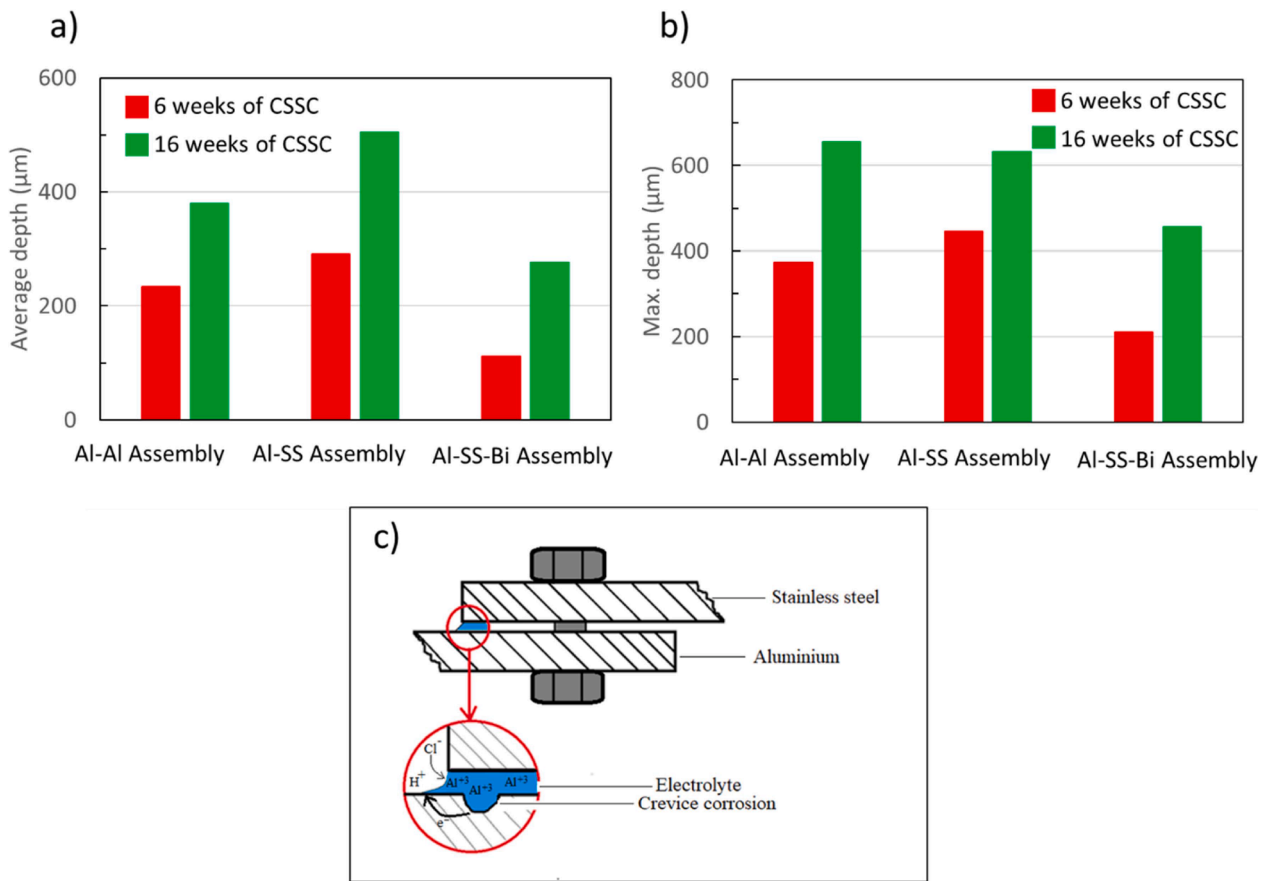


Fig. 13. a) Average depth of corrosion attack and b) maximum depth of corrosion attack measured on aluminium plates in Al-Al, Al-SS and Al-SS-Bi assemblies after 6 weeks (red) and 16 weeks (green) of CSSC testing. c) Schematic of crevice corrosion induced galvanic by the formation of a galvanic cell.

are polarized to $\approx -1.8 V_{(SHE)}$ or lower.

By comparing the measurements of the depth of corrosion attack for Al-Al assembly and Al-SS assembly (Fig. 13a and b), the difference of attack depth is not as extreme as the difference of weight loss. The reason for this is that the surface is directly affected by the galvanic difference between these two alloys, not the inside of ongoing (propagating) attacks where the environment and the electrochemical potential is less affected by the bulk environment. Inside the pit, the

environment will change dramatically from the bulk with respect to pH, and the content of chlorides in this case. This is illustrated in Fig. 13c. When chloride ions are present in an electrolyte, the situation worsens leading M^+ to attract Cl^- from the bulk (ref. electroneutrality), forming metal chlorides which hydrolyses to form metal hydroxide (MeOH) and hydrochloric acid (HCl). Hence, when a local attack is formed, it will rapidly start "living its own life" independent from the electrolyte outside the attacks as well as the electrochemical throwing power

caused by the galvanic difference between aluminium and stainless steel. Nevertheless, the depth is somewhat deeper in aluminium connected to stainless steel. This is often related to the shape of the pits and the local attacks, i.e., if the opening of the attack is wide or narrow. For pitting corrosion, e.g., ASTM G46 has developed a pitting characterization practice in which the density, the size, the depth, and the opening of the pits are used to define a so-called pit rating number for a certain alloy in a given environment. This examination has not been conducted in this study, but it is believed that the pits are not very narrow and will therefore allow some replacement of the environment inside the pit. If so, the outside conditions will increase the local corrosion rate somewhat if galvanically connected to a more noble alloy like stainless steel.

For Al-SS-Bi assembly, it is found that both average and maximum corrosion depth of the local corrosion attacks (pits) in the main aluminium plate are significantly less than the attacks on the Al-Al and the Al-SS setup. The reason for this is that the corrosion process is taking place on the aluminium part of the bimetallic plate as well as the aluminium washer underneath the bolt head on the aluminium side and thereby act as "sacrificial components" in this setup. To control the corrosion in a setup like this, the type of aluminium alloy in these

sacrificial components should be chosen with care. In the experiments reported herein, they have the same composition as the main plate. However, by selecting a more corrosion resistant (noble) alloy, this may lead to the same effects as for the Al-SS system. By selecting a less noble alloy, it will be a risk of structural failure (loss of torque, loosening, etc.) as the corrosion rate will be high due to the galvanic corrosion in addition to the self-corrosion.

Figs. 14, 15, and 16 document the differences in extent and type of corrosion between the three assemblies. As observed the difference between the 6 weeks and the 16 weeks cases are not significant for the three assemblies in term of pattern compared to the difference in term of weight loss and depth of attack. The galvanic corrosion process depends on the thickness of the aqueous salty film, which affects ohmic resistance. The thinner an aqueous salty film is the higher resistance and lower galvanic current will flow in the closed galvanic circuit, i.e., resulting in less galvanic corrosion. Therefore, for thin salty water film like in this experiment, the corrosion attacks are mainly located close to the very first few millimetres from the circumference of the washers. For a completely submerged system, the extent of these attacks would have been located even further away from the washers.

The "Internal surfaces" photos in Figs. 14 and 15, show that this

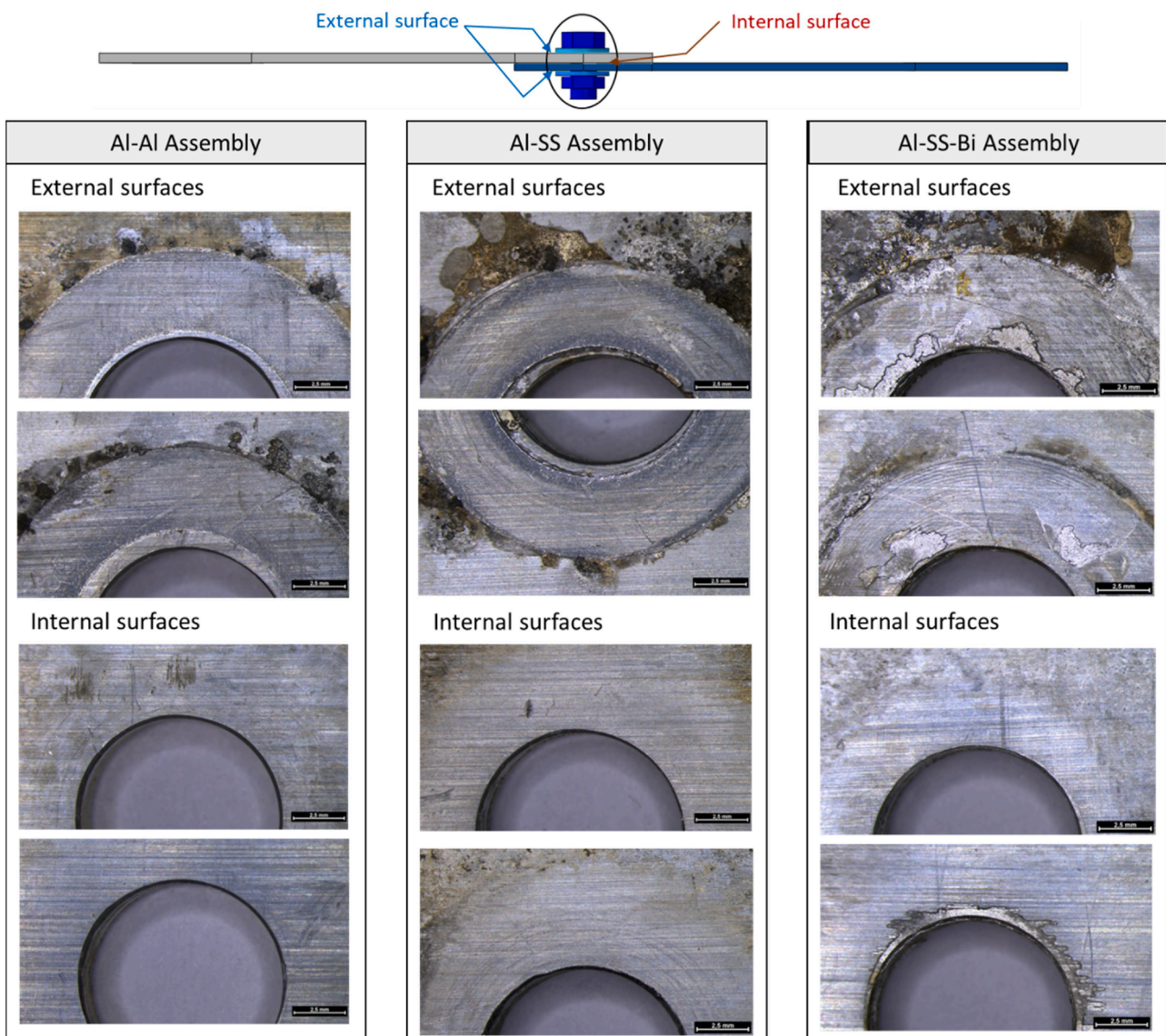


Fig. 14. Optical images showing corrosion attack in aluminium plate in the areas around the bolt on the external and internal surfaces of the assemblies after 6 weeks of CSSC testing.

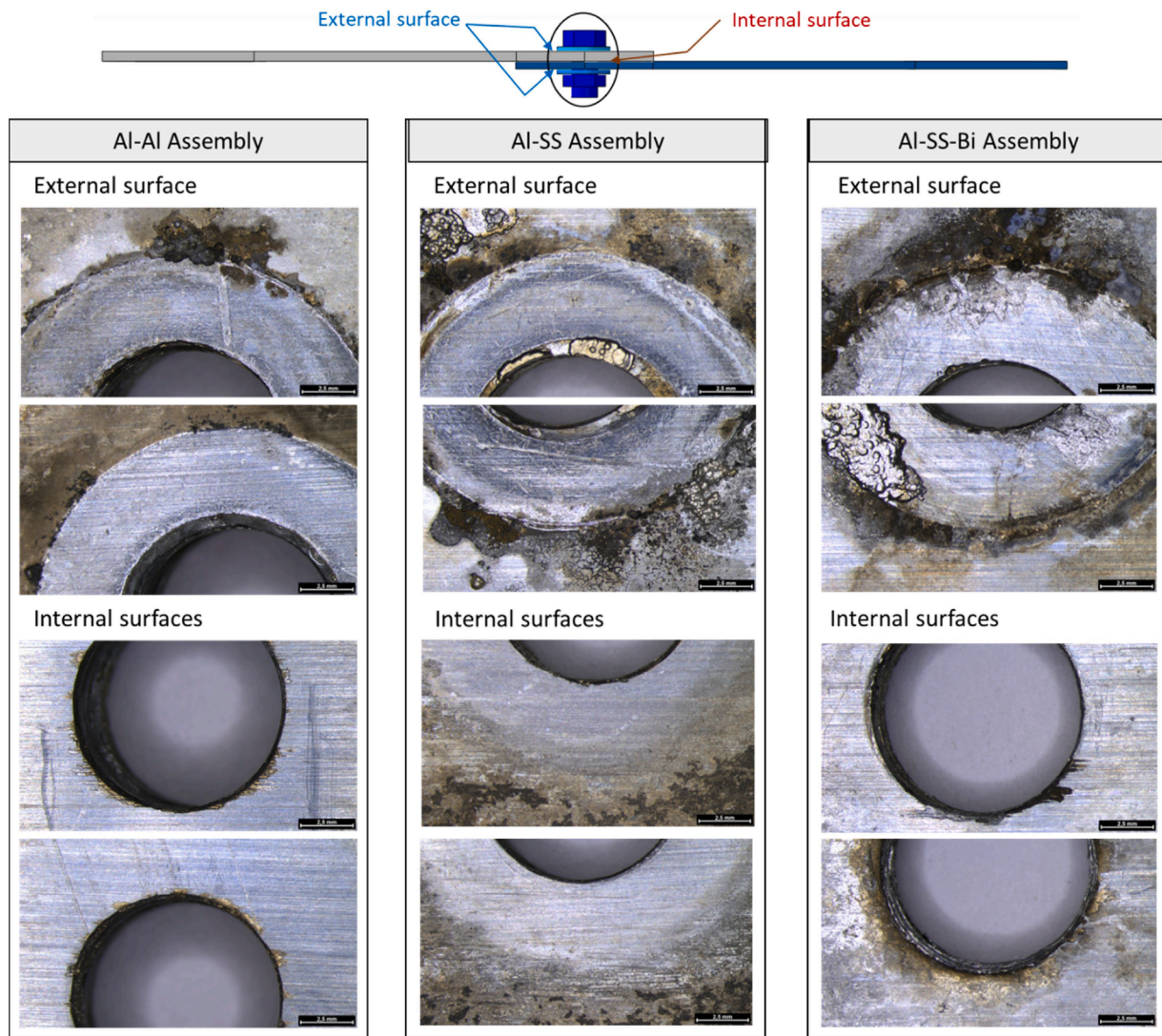


Fig. 15. Optical images showing corrosion attack in the areas around the bolt on the external and internal surfaces of the assemblies after 16 weeks of CSSC testing.

closed "compartment" area has not been exposed to fresh electrolyte and corrosion is prevented. If, for any reason, electrolyte penetrates these areas, significant corrosion is not expected due to high ohmic resistivity and very limited supply of fresh electrolyte with more chloride ions to feed the corrosion process.

The images in Fig. 16 are not significantly different from the "External surfaces" photos in Figs. 14 and 15 regarding corrosion mechanisms. However, by comparing the edge areas for Al-Al assembly vs. Al-SS and Al-SS-Bi assemblies, it is evident that galvanic corrosion takes place independently of the bolt, the washer, and the bimetallic plate. This is explained by the film thickness. For a thin film, the ohmic resistance will be high and the bolt and washer area will not influence the edge areas ≈ 10 mm away. Hence, the edges of the aluminium plates in Al-Al assembly are not affected while the edges of the aluminium plates in the Al-SS and Al-SS-Bi assemblies suffer from corrosion due to the stainless steel plate in direct electrical contact with the aluminium plate. However, the corrosion attack in the Al-SS assembly is more significant than the corrosion attack in the Al-SS-Bi assembly. As corrosion rate is defined as current divided by area, an edge will always lead to a higher current density and thereby increased corrosion as can be seen for the Al-SS and the Al-SS-Bi cases.

Tensile-shear test measurements

The introduction of bimetallic inserts in the Al-SS-Bi assembly affects

the tensile-shear force – displacement curve (Fig. 17), the failure mode of the aluminium plate (Fig. 20) and the rotation of the bolt (Fig. 18) compared to Al-SS assembly without bimetallic insert. Fig. 17 shows the load-displacement curves of the reference uncorroded assemblies. As can be observed, the contribution from the stainless steel plate increases the tensile-shear force of the Al-SS assembly compared to the Al-Al assembly. However, the incorporation of bimetallic insert in the Al-SS-Bi assembly reduces the tensile-shear forces prior to failure compared to the Al-SS assembly. This is explained by the effect of the bimetallic insert on the distribution of the forces in the assembly. As demonstrated in Fig. 18, the Al-SS-Bi assembly have the highest rotation due to increased lever arm (distance of applied loads from the plate interface) compared to Al-Al and Al-SS assemblies. These effects of bimetallic insert are further discussed in the Section 4.2.1 based on the results of FE simulations.

The effect of corrosion on the force - displacement curve depends on the assembly's setting as demonstrated in Fig. 19. The corrosion increases the tensile-shear forces of Al-Al and Al-SS assemblies compared to the reference measurements in dry condition. This increase was found to be independent on the duration of corrosion tests (6 weeks and 16 weeks). The Al-Al assembly has higher increase of force compared to the Al-SS assembly at similar displacement. The increase in tensile-shear force might be related to the formation of aluminium corrosion products. When the corrosion takes place, the corrosion products formed on

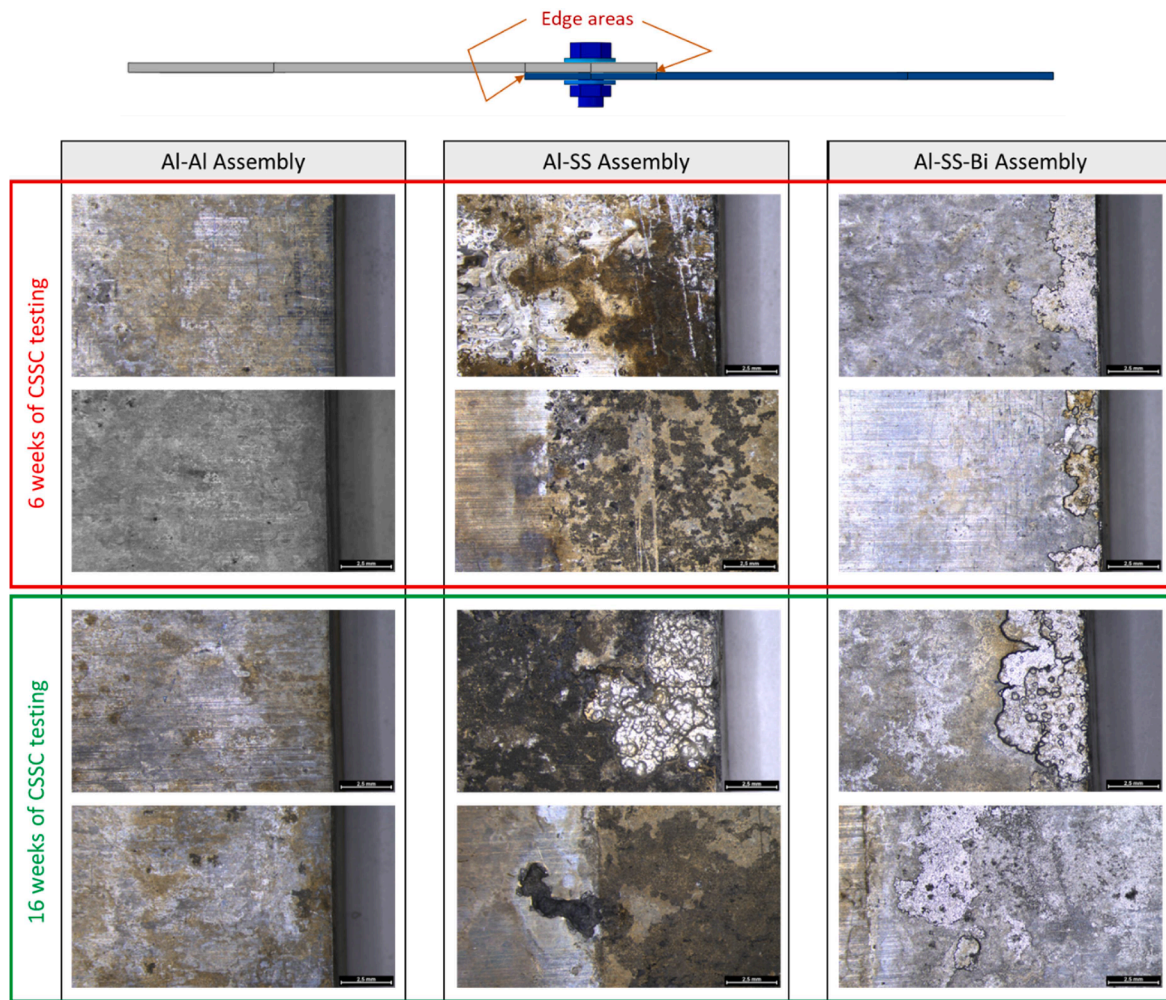


Fig. 16. Optical images showing corrosion attack in the areas closed to the plate's edges after 6 weeks and 16 weeks of CSSC testing.

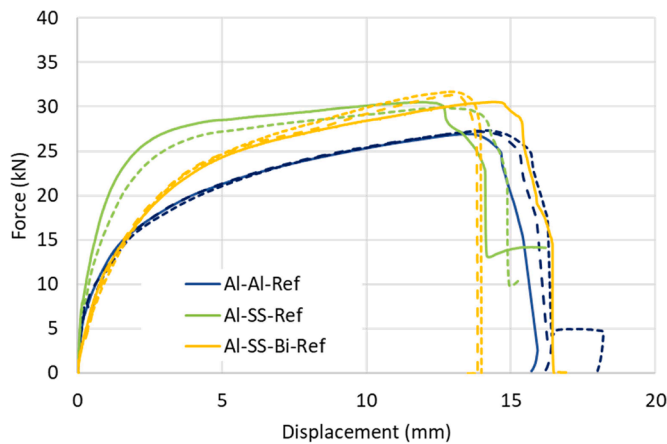


Fig. 17. Reference force-displacement curves determined by tensile-shear tests on the reference uncorroded assemblies including, aluminium-aluminium (Al-Al), aluminium-stainless steel (Al-SS) and aluminium-stainless steel with bimetallic insert (Al-SS-Bi).

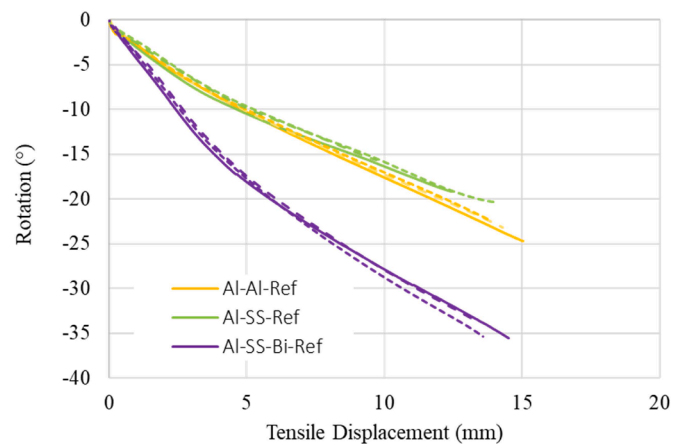


Fig. 18. Bolt's rotation during tensile-shear tests on the reference uncorroded assemblies including, aluminium-aluminium (Al-Al), aluminium-stainless steel (Al-SS) and aluminium-stainless steel with bimetallic insert (Al-SS-Bi).

the surface of aluminium plates increase the preload and frictional forces leading to increased contribution to the tensile-shear force in the corroded assemblies. The Al-Al assembly has two aluminium plates in contact with the stainless steel bolt and washer resulting in higher contributions to frictional response compared to Al-SS assembly, which

has one aluminium plate in contact with the stainless steel bolt and washer. Accordingly, the increase in the tensile-shear force for Al-Al assembly is higher than the increase in the tensile-shear force for the Al-SS assembly. This will be further discussed in the next section based on the FE simulations results. In the Al-SS-Bi assembly, the contact surface of the aluminium plate is protected by the sacrificial plate

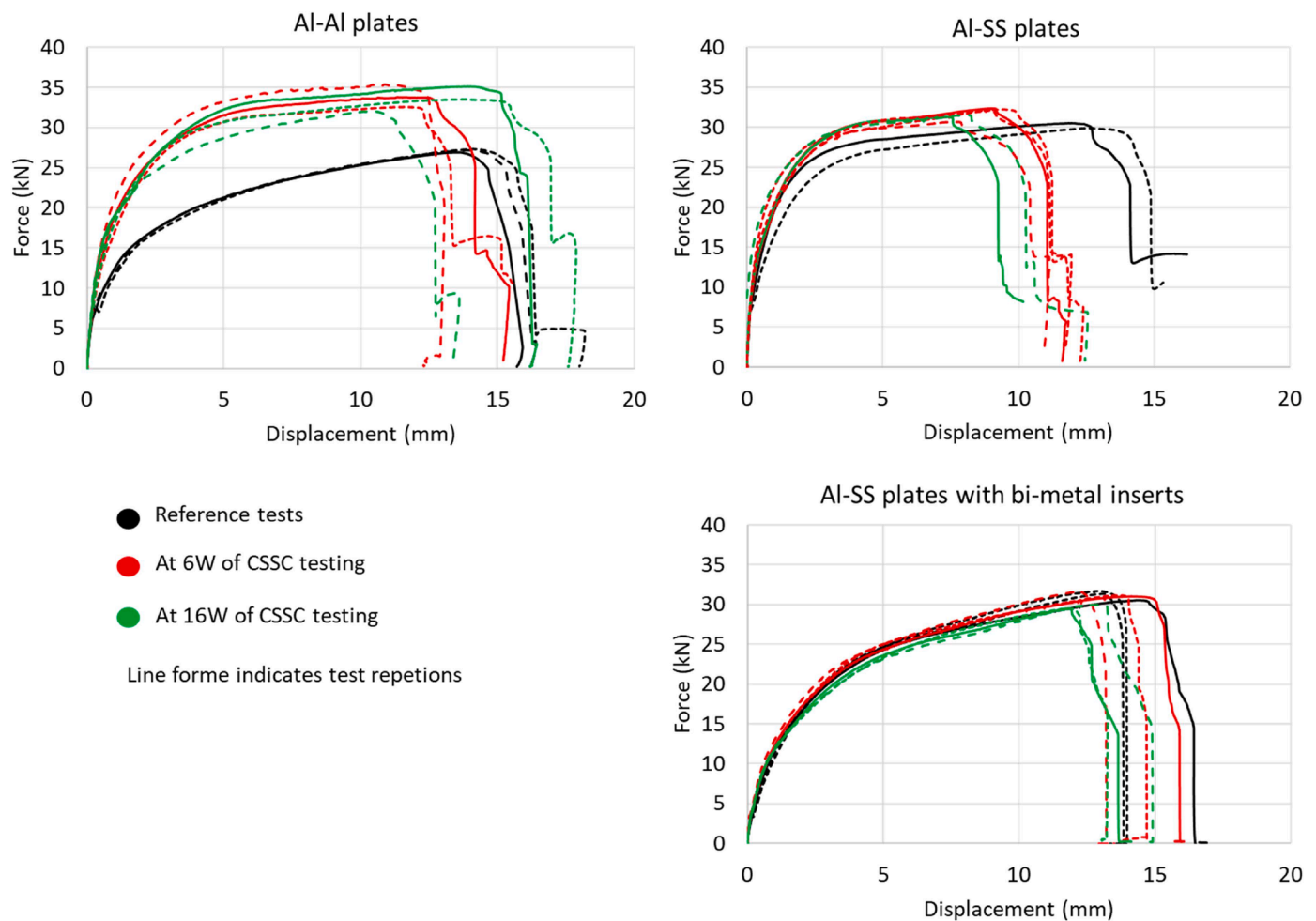


Fig. 19. Effects of corrosion on the force-displacement curves: black lines represent reference uncorroded assembly testing, red lines represent the tensile-shear test at 6 weeks of CSSC and green lines represent the tensile-shear tests at 16 weeks of CSSC.

components in the inserts and aluminium washer. The corrosion production is mainly formed on the aluminium part of the bimetallic insert, which is not constrained by the tensile-shear displacement or rotation. This will lead to similar frictional forces resulting in unaffected tensile-shear force for Al-SS-Bi assembly.

The displacement at failure is clearly decreased for Al-SS assembly without bimetallic insert (Fig. 19). In accordance with corrosion observations, the Al-SS has the highest weight loss, which increases material damage, creates local defects, and consequently promotes fracture of aluminium plate. This effect is less pronounced for Al-Al and Al-SS-Bi assemblies which have lower corrosion rate.

Fig. 20 shows the failure modes of the investigated assemblies before and after corrosion tests. The failure of the Al-Al and Al-SS reference assemblies (Fig. 20) is mainly dominated by the fracture of aluminium plates. The observed failure modes of all test repetitions were bearing and shear out type. The introduction of bimetallic insert changes the failure mode to net tension in the specimens where the bolts do not fail. The increase of lever arm increases the applied couple and the tension of the bolt, leading to bolt failure in some Al-SS-Bi assembly specimens. The assembly Al-SS-Bi requires bolt with higher strength to accommodate the increase in tension force associated with the introduction of the bimetallic insert. The corrosion seems to also affect the failure mode. The initiation of failure with net tension mode is observed in Al-Al assembly. This might be explained by the initiation of local defects and the increase of frictional force which promote fracture propagation in different mode compared to the reference assembly.

As shown in Fig. 21, the corrosion seems to have moderate effects on

the bolt rotations. The corrosion effect on the bolt rotation can be related to the changes in the preload and frictional forces as will be discussed in the next section. In agreement with the effects on tensile-shear forces, the Al-Al assembly has higher increase in the bolt rotation than the Al-SS assembly, while the rotation variation of Al-SS-Bi assembly is negligible.

Results of FE simulations

FE simulations VS experimental reference tests

Figs. 22 and 23 show the force-displacement curves and the failure modes as predicted by the FE simulations for Al-Al assembly, Al-SS assembly, and Al-SS-Bi assembly. In these simulations, the reference values of preload $F_n = 23$ kN was considered in all assemblies. The friction coefficients were adjusted based on the experimental measurement of tensile-shear of Al-SS assembly. The values of $\mu_{Al-Al} = 0.2$, $\mu_{Al-SS} = 0.14$, and $\mu_{Al-SS} = 0.1$ were considered in the simulations of Al-Al and Al-SS-Bi assemblies at dry condition. As can be observed, the simulations fairly predict the force displacement curves of Al-SS assembly and Al-SS-Bi assembly compared to experimental measurements. However, the FE simulation of Al-Al assembly overestimates the force-displacement curve compared to experimental measurement. There are different factors affecting the results of the FE simulations, including boundary conditions (preload and contact) and material models (yielding, hardening and damage). The same initial torque was applied on all assemblies in the FE simulation in accordance with experiments. The friction coefficient was calibrated based on the experimental measurements of Al-SS assembly, while the material models were calibrated

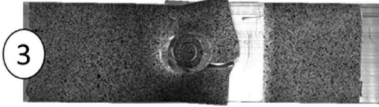
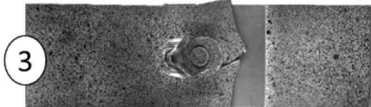
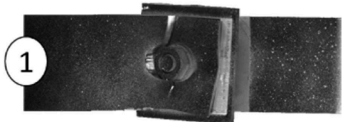

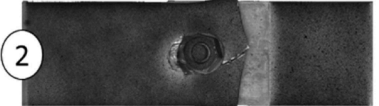
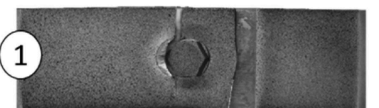
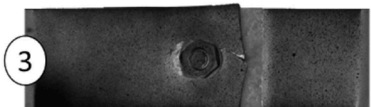


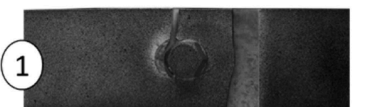
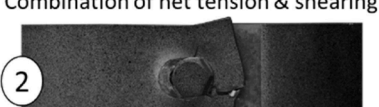
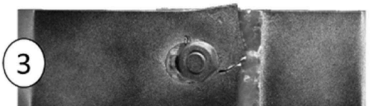
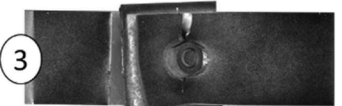
	Al-Al Assembly	Al-SS Assembly	Al-SS-Bi Assembly
Reference tests	<p>Bearing and shear out</p> 	<p>Bearing and shear out</p> 	<p>Net tension</p>  <p>Bolt failure</p> 
At 6 weeks of CSSC testing	<p>Bearing and shear out</p>  <p>Net tension</p> 	<p>Bearing and shear out</p> 	<p>Net tension</p>  <p>Bolt failure</p> 
At 16 weeks of CSSC testing	<p>Net tension</p>  <p>Combination of net tension & shearing</p> 	<p>Bearing and shear out</p> 	<p>Net tension</p> 

Fig. 20. Failure modes of the three assemblies after tensile-shear tests performed according to the chronological arrangement in Fig. 3. Encircled numbers indicate the amount of specimens associated to the associated damage.

based on tensile tests of Al and SS. The deviation between the FE results and the experimental measurement for Al-Al assembly might be explained by the simplified calibration model of aluminium, especially the failure envelope. Aluminium deformation is known to involve complex deformation mechanism, where advanced material model might be required (Saai et al., 2013; Saai et al., 2011a; Saai et al., 2011b). The simplified calibration process based on only tensile test might have higher consequence on the response of Al-Al assembly, due to the contributions of complex deformation mode in the two aluminium plates. Enhanced material model with improved calibration process using tensile, shear and biaxial test is highly recommended to improve the simulations results. However, the current FE simulations fairly predict the effects of the assembly settings on the force-displacement curves and on the failure mode in accordance with experimental observations. They demonstrate the influences of bimetallic insert in terms of lowering the yielding force of Al-SS-Bi assembly compared to the yielding force of Al-SS assembly and changing the failure mode from bearing and shear out type in Al-Al and Al-SS assemblies to net tension failure mode in Al-SS-Bi assembly, which agrees with experimental observations. As demonstrated in Fig. 24, the bimetallic insert significantly increases the bolt rotation compared to Al-Al and Al-SS assemblies. This is due to the increased lever arm of the applied couple resulting from the added insert thickness. At equivalent displacement, the bolt in the Al-SS assembly showed the highest shearing deformation and strain location in the contact area with the plates which is mainly related stress distribution in the connection.

Effects of preload and frictional forces

Increased tensile-shear forces were observed after the corrosion tests for Al-Al assembly and Al-SS assembly due to the formation of corrosion products on the aluminium plates. As discussed in Section 4.1, the corrosion products increase the preload of the bolts due to the related volume expansion. They also increase the frictional forces of the contact due to the increased pressure and the modification of the contact surface. An increased friction due to corrosion was observed in many tribo-corrosion studies on materials such as aluminium and stainless steel (Zhang et al., 2015; Li et al., 2021; Zhang et al., 2018). However, the synergistic effects of contact pressure and friction makes it difficult to describe their contributions to the tensile-shear force of the corroded assemblies. Experimental measurement of such dependency is complicated as it involves different material interfaces with various pressure and length scales. It is difficult to define a setup for friction test which represent the contact and friction conditions between the plates in the assembly. This motivated us to investigate this numerically. The focus herein is on the Al-Al and Al-SS assemblies, where the corrosion products affect the response of the bolted connection. First, the FE simulations were performed at two preload forces $F_n = 10\text{ kN}$ and $F_n = 30\text{ kN}$ without varying the friction coefficients ($\mu_{Al-Al} = 0.2$, $\mu_{Al-SS} = 0.14$ and $\mu_{SS-SS} = 0.1$). Then, the FE simulations were performed with increased friction coefficients of the contact areas involving aluminium. The friction coefficients were increased from 0.2 to 0.9 for μ_{Al-Al} and from 0.14 to 0.4 for μ_{Al-SS} . A higher increase in the value of μ_{Al-Al} was assumed to replicate the contributions from two aluminium plates in Al-Al assembly. The values of the preload and the friction coefficient

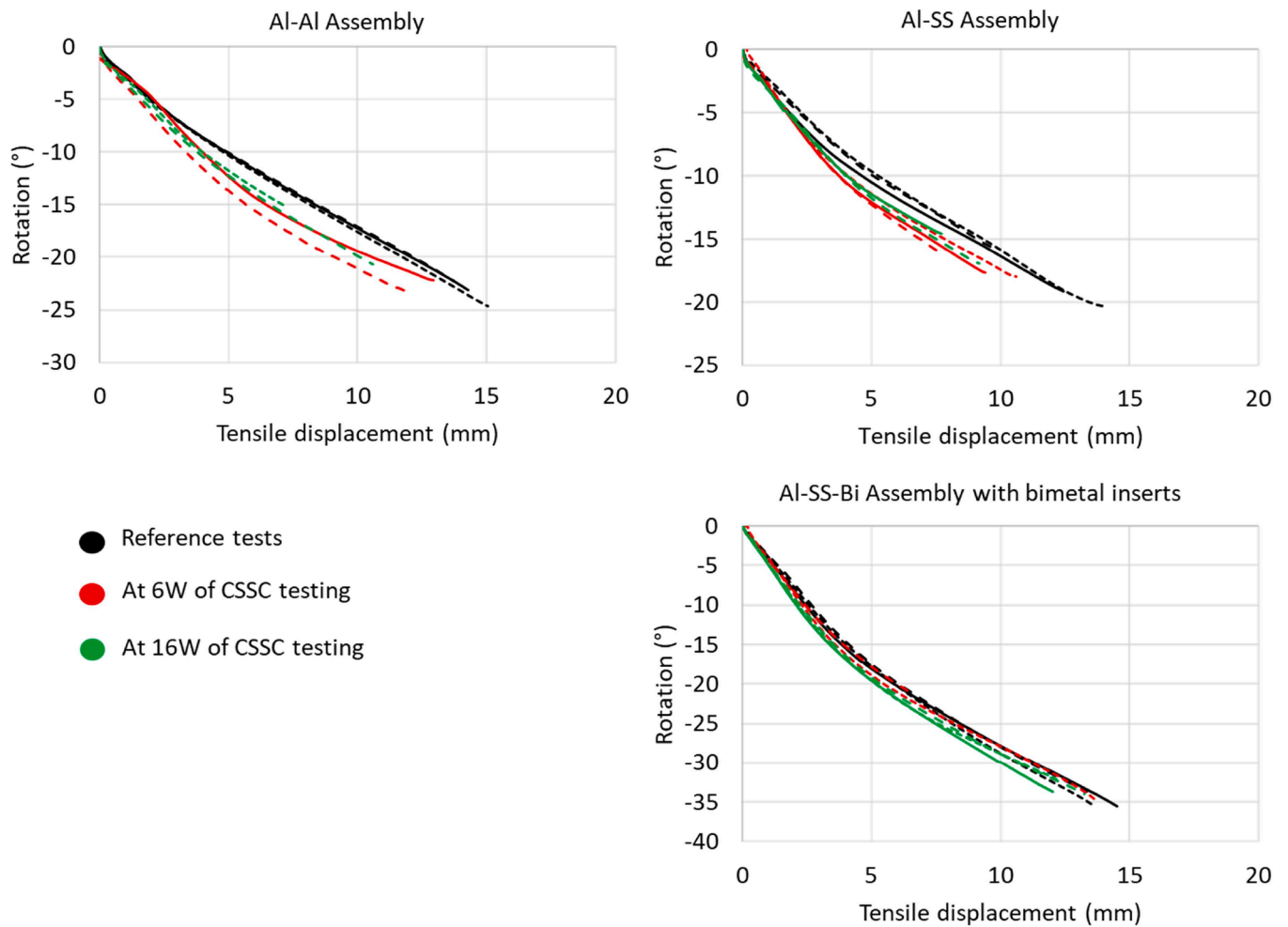


Fig. 21. Effects of corrosion on bolt rotation during tensile-shear tests: black lines represent reference uncorroded assembly testing, red lines represent tensile-shear test at 6 weeks of CSSC and green lines represent tensile-shear tests at 16 weeks of CSSC.

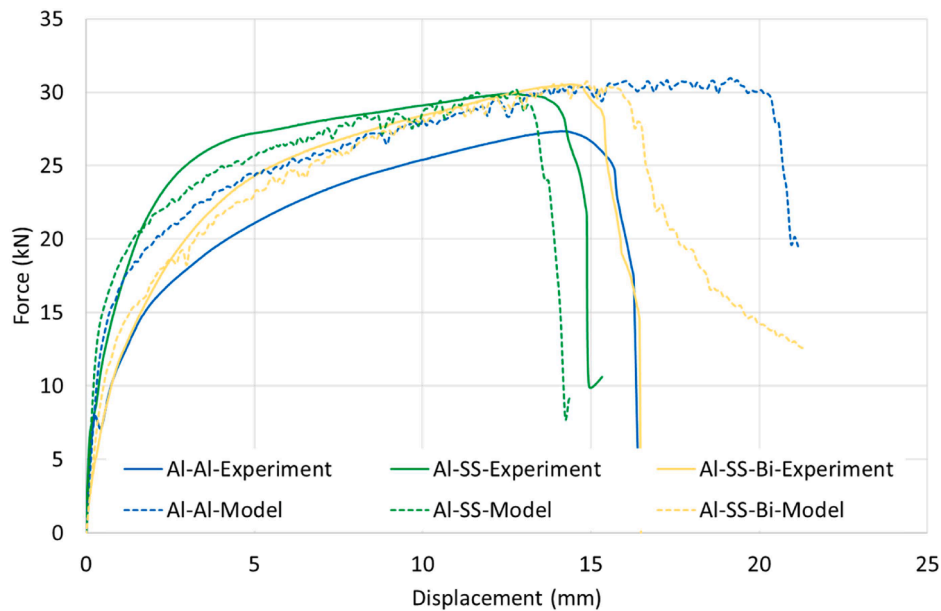


Fig. 22. Force-displacement curves predicted by FE simulations (dashed lines) versus experimental measurements (continuous lines) for aluminium-aluminium assembly (blue lines), aluminium-stainless steel assembly (black lines), and aluminium stainless steel with bimetallic insert assembly (red lines).

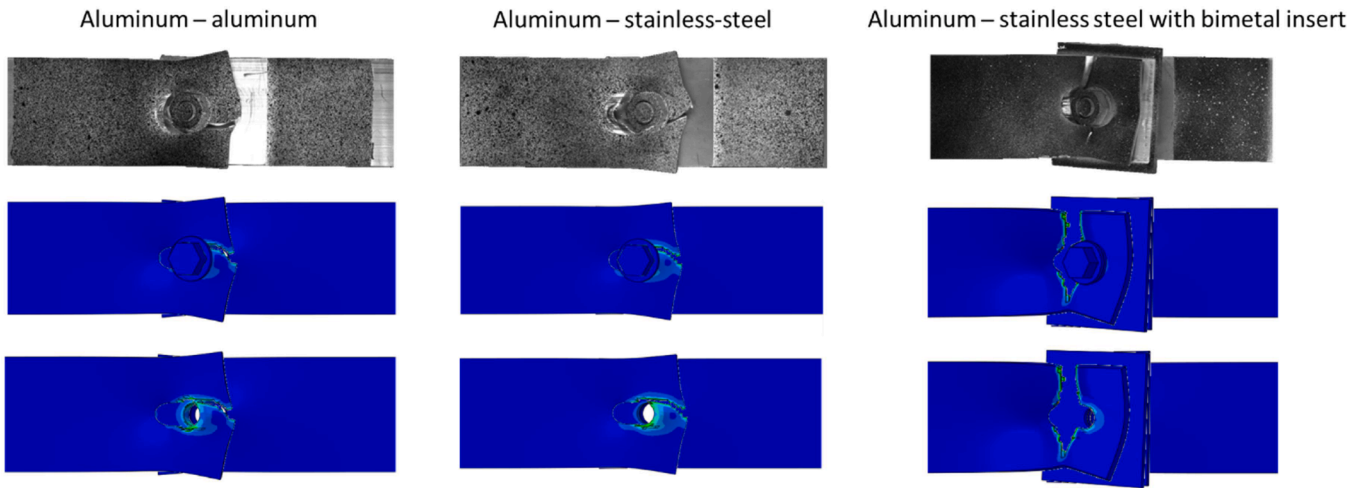


Fig. 23. Failure of bolted connections as predicted by FE simulations versus experimental observations.

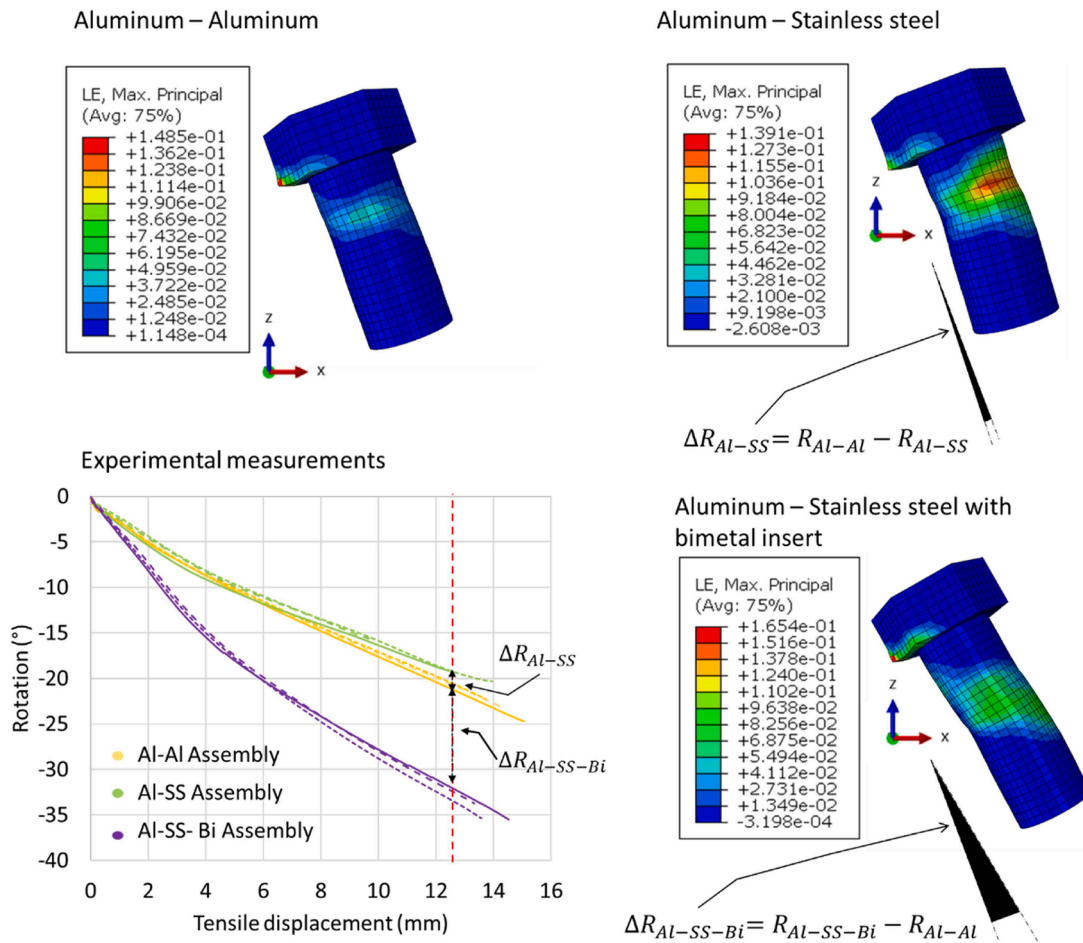


Fig. 24. Rotations and deformations of bolts as predicted by the FE simulations at equivalent tensile displacements of 12.5 mm. Black angles represent the rotation differences ΔR of aluminium-stainless steel assemblies compared to aluminium-aluminium assembly.

μ_{SS-SS} in the second simulations were kept the same as the reference values ($F_n = 23 \text{ kN}$ and $\mu_{SS-SS} = 0.1$).

Fig. 25 shows the effects of the preload on the tensile-shear force and on the contact pressure. As can be observed, the increased preload with constant friction coefficients increases the initial contact pressure. Without increasing the friction coefficients, this leads to small increase in the tensile-shear force at very early stage of tensile-shear

displacement. After 2 mm of displacement, the increase in contact pressure is dominated by the plate deformation. Due to the bolt rotation and plate deformation, the contact areas are modified during testing. The contact pressure in the nodes increases only when they are in the contact area constrained by the nut and the bolt head. This involves variation in the contact pressure in the nodes due to flow of material during tensile-shear displacement. When increasing the friction

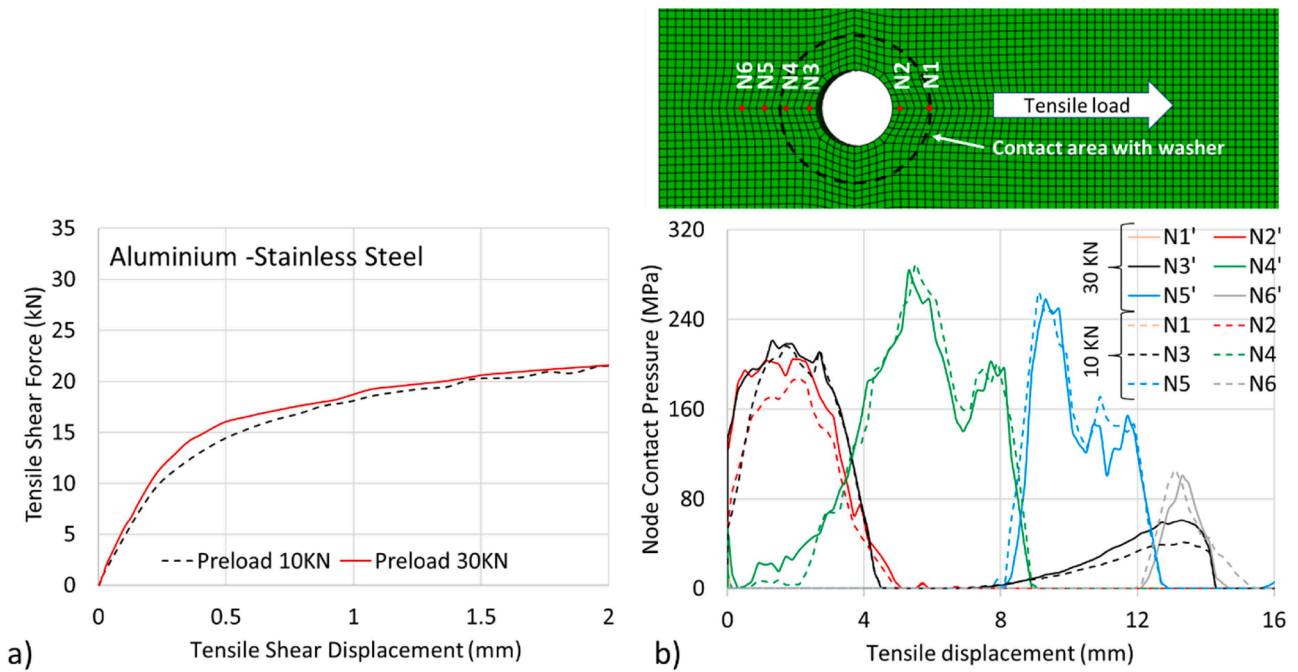


Fig. 25. Effect of preload on a) tensile-shear force on aluminium-stainless steel assembly and b) contact pressure of nodes N1-N6 of aluminium plate distributed on the midline of aluminium-stainless steel contact surface around the bolt (see upper image).

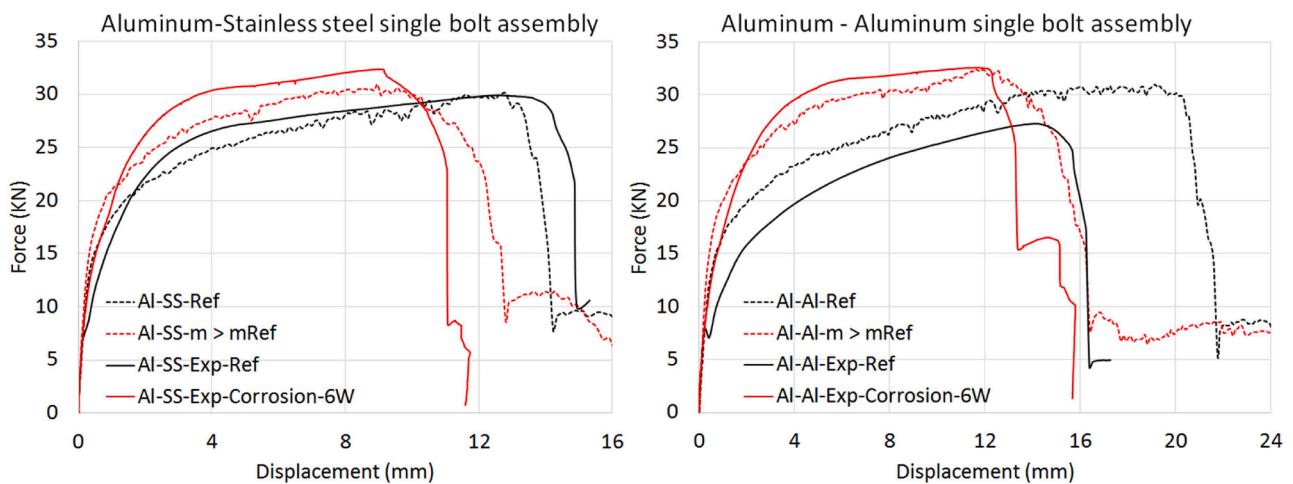


Fig. 26. Effect of friction on tensile-shear forces (continuous lines) compared to experimental measurements (dashed lines) of reference assemblies (in black) and 6 weeks corroded assemblies (in red).

coefficient at a constant preload, a significant increase in the tensile-shear forces is observed on the FE simulation results (see Fig. 26). This is due to the direct contribution of friction coefficients to the frictional force and consequently to the tensile-shear force. The increase in frictional force also affects the displacement at failure. The increased frictional force contributes to the localization of deformation, leading to earlier initiation of damage in aluminium plates (see Fig. 27). Another interesting observation is the effects of increased frictional forces on the bolt rotation (see Fig. 28). The increased resistance to relative displacement in the contact causes an increase in the rotation of the bolt to accommodate for tensile-shear displacement. This agrees with experimental measurements, which also highlight a small increase in the rotation of the bolts for Al-Al assembly and Al-SS assembly resulting from the effect of corrosion product (see Fig. 21).

In Fig. 26, the FE simulations predict higher increase in the tensile-shear forces for Al-Al assembly compared to Al-SS assembly, which

agrees with experimental observations. This might confirm the assumption that the corrosion products formed on the aluminium surface have the major contribution to the frictional force, where the higher increase of μ_{Al-Al} compared to the increase of μ_{Al-SS} replicate the contribution from the two aluminium plates to the contact frictional forces.

Discussion

The measurements of tensile-shear test and the corrosion characterizations demonstrated significant effects of corrosion on the strength and the damage of Al-Al and Al-SS assemblies. The introduction of bimetallic inserts in the Al-SS-Bi assembly reduced the effects of corrosion. It however affects the strength of the Al-SS-Bi assembly compared to the Al-SS assembly. The introduction of bimetallic inserts affects the tensile-shear force – displacement curve (Fig. 17), the failure mode of

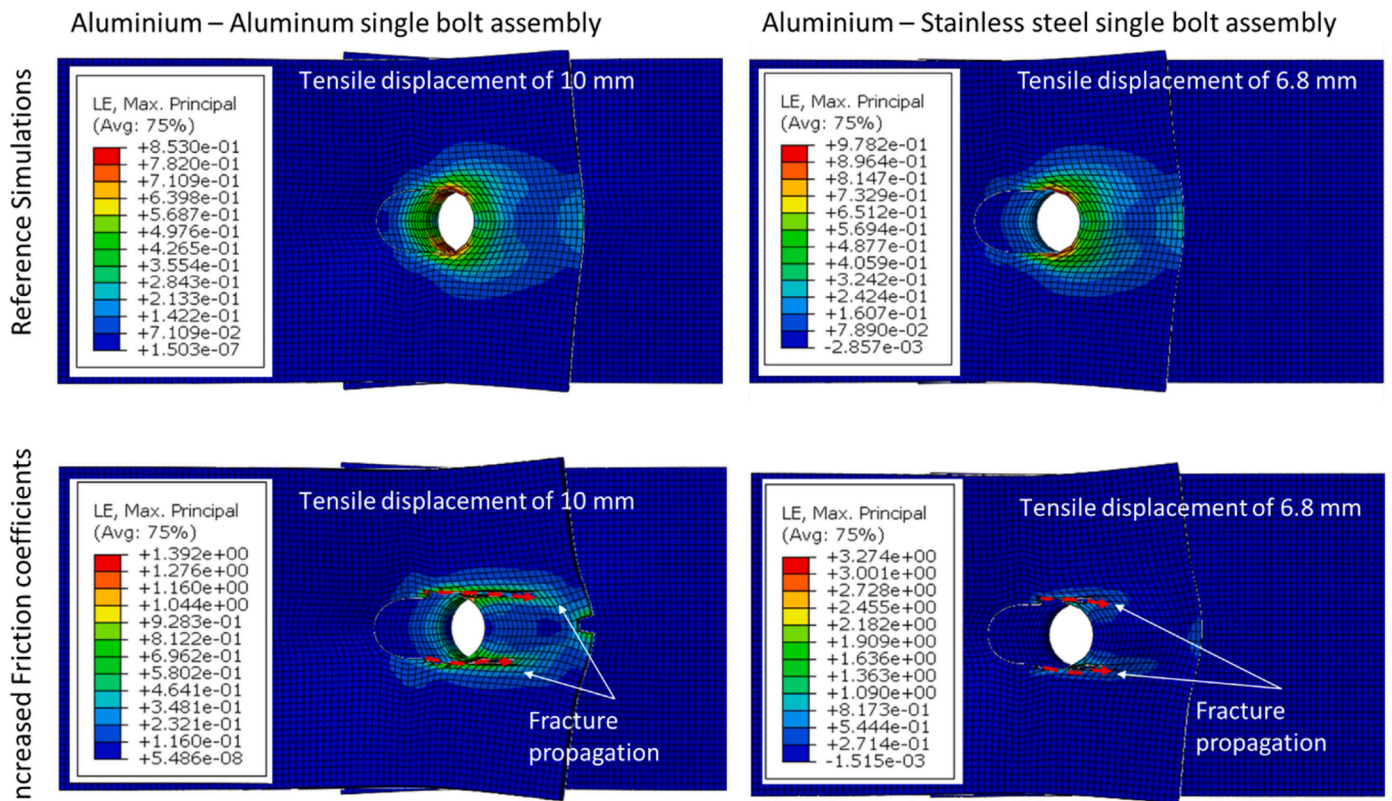


Fig. 27. Effect of increased friction coefficient on the deformation of aluminium plates at equivalent displacements in Al-Al and Al-SS assemblies.

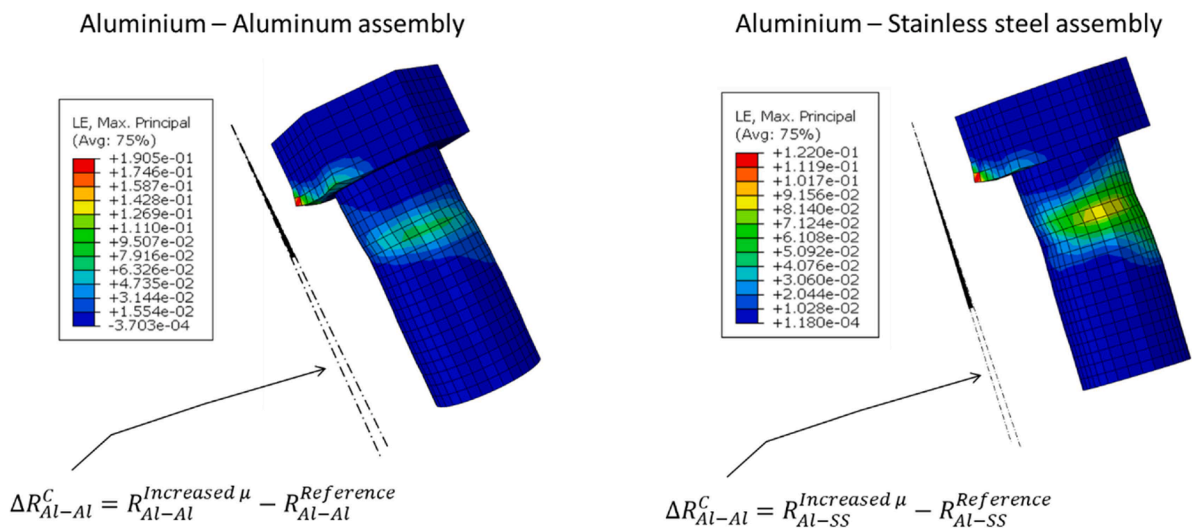


Fig. 28. Effects of increased friction on rotation and local deformation of bolts in Al-Al and Al-SS assemblies.

the aluminium plate (Fig. 20) and the rotation of the bolt (Fig. 18). Considering that there is no adhesion between the bimetallic insert and the plates, the frictional contact with the insert is limited to the contact area with the plates. The insert mainly affects the thickness of the assembly and consequently the bolt rotation and the force distribution. As demonstrated in Fig. 18, the Al-SS-Bi assembly has the highest rotation due to increased lever arm compared to Al-Al and Al-SS assemblies. This might explain the reduction in the tensile-shear force prior to failure compared to the assembly without bimetallic insert. Such effects of bimetallic inserts must be considered during the design phase of dissimilar material bolted connection.

The consequences of corrosion on the mechanical response of the

assembly are I) material loss causing locale defects and affecting the contact and II) formation of corrosion products, which requires extended volume and thereby increases the contact force and the tension in the bolt. The friction coefficient is an important parameter which might describe the effect of corrosion on the strength of the assembly (Fig. 26). It however depends on the synergistic effects of the preload and the contact conditions which both are modified due to corrosion. This dependency is difficult to be described by experimental set up. Based on numerical simulations, the contact pressure was found to depend not only on the preload, but also on the plate deformation which have dominated effects at high tensile-shear displacement (Fig. 25). The tensile-shear forces computed by the FE simulations in this study are

more sensitive to the effect of friction coefficient, which has direct impacts on the frictional forces leading to significant increase in the tensile-shear forces. Therefore, a pressure-dependent friction coefficient is recommended to describe the frictional response of the preloaded connection. However, the main limitation of pressure-dependent frictional model is the difficulty to describe the dependency on the pressure for both uncorroded bolted assemblies and corroded bolted assemblies.

Fig. 19 showed that the displacements at failure of Al-SS assembly are significantly affected by the galvanic corrosion. All testing parallels after 6 and 16 weeks result in approximately 20 % less displacement at damage than the uncorroded reference assembly. This is consistent with corrosion observations, where the Al-SS assembly have the highest weight loss and the highest depth of corrosion attack. The corrosion creates local defect in the aluminium plate promoting fracture. The introduction of bimetallic insert reduced the corrosion attack of the aluminium plate. This explains the lower effects of corrosion on the displacement at failure for Al-SS-Bi Assembly.

Another interesting observation is the increase of tensile-shear forces of the corroded Al-Al and the corroded Al-SS assemblies (Fig. 19). This was explained by the effect of aluminium corrosion products on the frictional forces, which act like a kind of "glue" increasing the resistance to sliding. The highest increase in tensile-shear force was associated to the Al-Al assembly. This was related to the contribution from two aluminium plates to corrosion production, leading to higher increase in the frictional forces (Fig. 26). The Al-SS-Bi assembly has quite similar force-displacement curves for the corroded and non-corroded reference setups (Fig. 19). The reason is most likely that the contact surface of the aluminium plate is protected by the sacrificial plate/washer components in the inserts. This will lead to similar frictional forces and unaffected tensile-shear forces. In practice, this implies that the structural integrity for our case and the lifetime of the connection is most likely to be maintained under such corrosive conditions.

Corrosion observations of the bolted assemblies (Section 4.1.1) demonstrated that the extent of corrosion in terms of weight loss for the aluminium plates is much higher when connecting them to stainless steel plate which is significantly more noble than aluminium. For the adjusted pH of 8.2 in these experiments, aluminium is normally passive, but is susceptible to local corrosion like e.g., crevice corrosion and/or pitting corrosion, especially in the presence of chloride ions. Since this testing was conducted in a chloride containing environment, local corrosion will take place, and will initiate more frequent over the surface when the electrochemical potential is increased in electrical contact with the stainless steel. Hence, the total number of attacks, and thereby the total weight loss, will be higher for the aluminium plates in a galvanic contact with the stainless steel.

When it comes to the depth of the corrosion attacks, this mechanism is not particularly affected by the galvanic effect since the environment inside the attack is less dependent of the bulk environment when the attack has been initiated and propagates. During this phase, the attack will suck in the chloride ions from the bulk to establish the electro-neutrality. Then, the chloride ions will result in the formation of hydrochloric acid which gradually brings the pH below 4, meaning that the aluminium is no longer passive and starts to corrode actively ($\text{Al} \rightarrow \text{Al}^{3+}$). For the case with bimetallic inserts, the aluminium in the insert will act as a sacrificial component and thereby protect the main aluminium plate. However, this depends on the thickness of the electrolyte layer surrounding the system as well as the content of chlorides and ionic conductivity. For the testing herein, the salt spray will not form a massive electrolyte bulk, meaning that the galvanic currents flowing between the main aluminium plate and the stainless steel plate will be restricted (limited). This is important to have in mind if such a system is submerged in e.g., a saltwater system for periods. If so, the ionic resistance in the system will be less and cause corrosion of the aluminium plate as well as the aluminium in the bimetallic inserts.

Conclusion

The effects of bimetallic inserts on the corrosion and mechanical performance of aluminium – stainless steel lap shear bolted assemblies were investigated by comparative study combining experimental testing and numerical simulations. The tensile shear tests were performed on Al-SS, Al-SS-Bi and Al-Al assemblies in dry condition and at 2 corrosion states corresponding to 6 weeks and 16 weeks. The comparative study highlights the following key insights:

- Galvanic corrosion of bolted assemblies has consequences not only on the material damage represented by the weight loss, but also on the frictional response of the contacting surfaces. The corrosion products formed on the aluminium plates in the Al-Al and Al-SS assemblies is expected to increase the frictional force and consequently the tensile-shear force. Based on the experimental observations, this effect seems to depend on the contact areas with aluminium more than on the duration of the corrosion tests. The Al-Al bolted assembly with two aluminium plates has the highest increase in the tensile-shear force. An average increase of 28 % of the ultimate force is measured in the case of the Al-Al assemblies (From 27.2 to 35.0 kN), while it is 8.0 % in the case of the Al-SS assemblies (From 30.2 to 32.6 kN), and almost negligible in the presence of a bimetallic insert.
- The application of bimetallic inserts in Al-SS-Bi assembly prevents the corrosion production on the aluminium plates, leading to 62 % decrease of the average depth of the compared to the Al-SS assembly after 6 weeks and 55 % reduction after 16 weeks. However, the addition of bimetallic insert increases the thickness of the joint resulting in reduced yielding force, increased rotation and modified failure mode compared to Al-SS assembly without insert. For the lap shear single bolt setting with bimetallic insert in this study, the reduction of yield force measured at 2.5 mm was 26 % compared the setting without bimetallic insert, while the bolt rotation increased from 16° to 28°. This needs to be considered in the design of bolted joint with bimetallic insert.
- FE simulations demonstrated that the increase of the preload associated with the formation of corrosion products increases the initial pressure of the contact area below the washer in the Al-Al and Al-SS assemblies. However, the contact pressure during the tensile-shear load is mainly dominated by the deformation of the plates. The FE simulations with increased friction coefficients demonstrated an increase in the tensile-shear force due to increased frictional forces. The FE results are in agreement with experimental observations, where an increase of the tensile-shear force was observed for the corroded Al-Al and Al-SS assemblies.
- The effect of corrosion on the preload and the frictional force is important and needs to be considered when designing dissimilar material bolted assemblies.

Declaration of Competing Interest

The authors declare that they have no known competing financial interests or personal relationships that could have appeared to influence the work reported in this paper.

Data availability

No data was used for the research described in the article.

Acknowledgements

The authors acknowledge the financial support of this work from the Research Council of Norway through the Centre for Research-based Innovation (CRI) BLUES - Floating structures for the next generation ocean industries (grant agreement number 309281).

References

- ASTM B 117:2018 Standard practice for operating salt spray (Fog) apparatus.
- ASTM G 116 1999 Standard practice for conducting wire-on-bolt test for atmospheric galvanic corrosion.
- ASTM G104: 1989 Standard test method for assessing Galvanic corrosion caused by the atmosphere.
- ASTM G85:2019 Standard practice for modified salt spray (Fog) testing.
- Bai, Y., Wierzbicki, T., 2010. Application of extended Mohr-Coulomb criterion to ductile fracture. *Int. J. Fract.* 161, 1–20. <https://doi.org/10.1007/s10704-009-9422-8>.
- Bickford, J.H., 1995. *Introduction to the Design and Behavior of Bolted Joints: Non-Gasketed Joints*. CRC Press. Third edition.
- Boretzki, J., Albiez, M., 2023. Static strength and load bearing behaviour of hybrid bonded bolted joints: experimental and numerical investigations. *J. Adhes.* 99 (4), 606–631. <https://doi.org/10.1080/00218464.2022.2033619>.
- Calabrese, L.P., Proverbio E., Pollicino, G., Borsellino C. Effect of galvanic corrosion on durability of aluminium/steel self-piercing rivet joints. *Int. J. Corros. Process. Corros. Control* 50 1 (2015) 10–17. DOI: [10.1179/1743278214Y.0000000168](https://doi.org/10.1179/1743278214Y.0000000168).
- Del Real, J.C., Cano De Santayana, M., Abenojar, J., Martinez, M.A., 2006. Adhesive bonding of aluminium with structural acrylic adhesives: durability in wet environments. *J. Adhes. Sci. Technol.* 20, 1801–1818. <https://doi.org/10.1163/156856106779116614>.
- Delzendehrooy, F., Akhavan-Safar, A., Barbosa, A.Q., Carbas, R.J.C., Marques, E.A.S., da Silva, L.F.M., 2022. Investigation of the mechanical performance of hybrid bolted-bonded joints subjected to different ageing conditions: effect of geometrical parameters and bolt size. *J. Adv. Join. Process.* 5 <https://doi.org/10.1016/j.jajp.2022.100098>.
- Denkert, C., Kühne, D., Süße, D., Glienke, R., Fiedler, M., Dörre, M., Kästner, M., Henkel, K.-M., 2022. Numerical and experimental studies on press-bolt joints for sheet metal applications - Static strength assessment. *J. Adv. Join. Process.* 6 <https://doi.org/10.1016/j.jajp.2022.100132>.
- DIC Software, 2017. *Ecorr v4.0*. Copyright. NTNU, Egil Fagerholt.
- EN 1090-3:2019 Execution of steel structures and aluminium structures - part 3: technical requirements for aluminium structures.
- Gupta, S., Singh, D., Yadav, A., Jain, S., Pratap, B., 2020. A comparative study of 5083 aluminium alloy and 316 L stainless steel for shipbuilding material. In: *The 2nd International Conference on Advances in Mechanical Engineering and Nanotechnology*, Materials Today Proceedings, 28, pp. 2358–2363. <https://doi.org/10.1016/j.matpr.2020.04.641>.
- Haris, A., Tay, T.E., Tan, V.B.C., 2017. Experimental analysis of composite bolted joints using digital image correlation. *J. Mech. Eng. Sci.* 11 (1), 2443–2455. <https://doi.org/10.15282/jmes.11.1.2017.4.0225>.
- Hillerborg, A., Modder, M., Petersson, P.-E., 1976. Analysis of crack formation and crack growth in concrete by means of fracture mechanics and finite elements. *Cem. Concr. Res.* 6, 773–782. [https://doi.org/10.1016/0008-8846\(76\)90007-7](https://doi.org/10.1016/0008-8846(76)90007-7).
- Hu, Q., Zhang, F., Li, X., Chen, J., 2018. Overview on the prediction models for sheet metal forming failure: necking and ductile fracture. *Acta Mech. Solida Sin.* 31, 259–289. <https://doi.org/10.1007/s10338-018-0026-6>.
- ISO 11997-1: 2017, Paints and varnishes — determination of resistance to cyclic corrosion conditions — part 1: wet (salt fog)/dry/humid. Annex A— cycle A.
- ISO 12996:2013 (E) Mechanical joining - destructive testing of joints - specimen dimensions and test procedure for tensile shear testing of single joints.
- ISO 9227:2012 Corrosion tests in artificial atmospheres - Salt spray tests.
- Jiang, C., Xiong, W., Cai, C.S., Zhu, Y., Wang, J., 2022. Preload loss of high-strength bolts in friction connections considering corrosion damage and fatigue loading. *Eng. Fail. Anal.* 137, 106411. <https://doi.org/10.1016/j.engfailanal.2022.106411>.
- Jun, J., Lim, Y.C., Li, Y., Warren, C.D., Feng, Z., 2021. Mitigation of galvanic corrosion in bolted joint of AZ31B and carbon fiber-reinforced composite using polymer insulation. *Materials (Basel)* 14 (7), 1670. <https://doi.org/10.3390/ma14071670>.
- Kim, I.-T., Lee, J.M., Huh, J., Ahn, J.-H., 2016. Tensile behaviors of friction bolt connection with bolt head corrosion damage. *Exp. Res. B. Eng. Fail. Anal.* 59, 526–543.
- Kong, Z., Jin, Y., Hong, S., Liu, Q., Vu, Q.-V., Kim, S.-E., 2022. Degradation behavior of the preload force of high-strength bolts after corrosion. *Buildings* 12, 2122. <https://doi.org/10.3390/buildings12122122>.
- Kong, Z., Yang, F., Jin, Y., Hong, S., Wang, X., Vu, Q.-V., Truong, V.-H., Yu, B., Kim, S.-E., 2021b. Experimental study on bearing capacity of corroded high-strength bolt connections under shear force. *Constr. Build. Mater.* 309, 125117.
- Kong, Z., Yang, F., Jin, Y., Hong, S., Wang, X., Vu, Q.-V., Truong, V.-H., Yu, B., Kim, S.-E., 2021a. Experimental study on bearing capacity of corroded high-strength bolt connections under shear force. *Constr. Build. Mater.* 309, 125117 <https://doi.org/10.1016/j.conbuildmat.2021.125117>.
- Langoy, M., 2023. Review of structural connections of dissimilar metals – prevention of galvanic corrosion; practice and experience. *Petroleumstilsynet. Report Z-Pt-201*. <https://www.ptil.no/contentassets/2be164e3a83c47a6be00badec8d40d6/review-of-structural-connections-of-dissimilar-metals.-prevention-of-galvanic-corrosion—practice-and-experience>.
- Li, L., Li, Y., Shi, W., Li, C.-Q., 2021a. Deterioration of fatigue strength of bolted connection plates under combined corrosion and fatigue. *J. Constr. Steel Res.* 179, 106559 <https://doi.org/10.1016/j.jcsr.2021.106559>.
- Li, M., Yao, L., Zhang, S., Wang, D., He, Z., Sun, G., 2021c. Study on bolt head corrosion influence on the clamping force loss of high strength bolt. *Eng. Fail. Anal.* 129, 105660.
- Li, Z., Yu, H., Sun, D., 2021b. The tribocorrosion mechanism of aluminium alloy 7075-T6 in the deep ocean. *Corros. Sci.* 183, 109306 <https://doi.org/10.1016/j.corsci.2021.109306>.
- Lou, Y., Huh, H., Lim, S., Pack, K., 2012. New ductile fracture criterion for prediction of fracture forming limit diagrams of sheet metals. *Int. J. Solids Struct.* 49, 3605–3615. <https://doi.org/10.1016/j.ijsolstr.2012.02.016>.
- Lundberg, S., 2016. Use of aluminium structures in offshore industry. *Key Eng. Mater.* 710, 22–31. <https://doi.org/10.4028/www.scientific.net/KEM.710.22>.
- Mariam M., Afendi M., Abdul Majid M.S. 2017 The effect of dry and wet condition on the mechanical properties of hybrid single lap. *Joining and welding symposium*. 238. IOP Conf. Series: Materials Science and Engineering. DOI: [10.1088/1757-899X/238/1/012005](https://doi.org/10.1088/1757-899X/238/1/012005).
- Martinsen, K., Hu, S.J., Carlson, B.E., 2015. Joining of dissimilar materials. *CIRP Ann. - Manuf. Technol.* 64, 679–699. <https://doi.org/10.1016/j.cirp.2015.05.006>.
- Meikle, T., Tadolini, S.C., Sainsbury, B.-A., Bolton, J., 2017. Laboratory and field testing of bolting systems subjected to highly corrosive environments. *Int. J. Mining Sci. Technol.* 27, 101–106. <https://doi.org/10.1016/j.ijmst.2016.11.017>.
- Melhem G.N. (2019) *Aerospace fasteners: use in structural applications*. Encyclopedia of aluminum and its alloys, first edition. DOI: [10.1201/9781351045636-140000240](https://doi.org/10.1201/9781351045636-140000240).
- Montemor, M.F., 2016. Corrosion issues in joining lightweight materials: a review of the latest achievements. *Phys. Sci. Rev.* 1, 20150011 <https://doi.org/10.1515/psr-2015-0011>.
- NORSK Standard – M-001: 2014/A1:2021. Amendment- material selection, annex B: implementation and use of the standard guidance for design of dissimilar metal connections.
- NORSOK Standard - M-102:2015 Structural aluminium fabrication.
- Pater, Z., Tomczak, J., Bulzak, T., Wojcik, L., Walczuk, P., 2020. Assessment of ductile fracture criteria with respect to their application in the modeling of cross wedge rolling. *J. Mater. Process. Technol.* 278, 116501 <https://doi.org/10.1016/j.jmatprotec.2019.116501>.
- Pourbaix, M., 1966. *Atlas of Electrochemical Equilibria in - Aqueous Solutions, 1st English Edition*. Pergamon Press Ltd. Second English Edition 1974 National Association of Corrosion Engineers.
- Saai, A., Dumoulin, S., Hopperstad, O.S., 2011a. Influence of texture and grain shape on the yield surface in aluminium sheet material subjected to large deformations. In: *The 14th International ESAFORM Conference on Material Forming AIP Conf. Proc.* 1353, pp. 85–90. <https://doi.org/10.1063/1.3589496>.
- Saai, A., Dumoulin, S., Hopperstad, O.S., Lademo, O.-G., 2013. Simulation of yield surfaces for aluminium sheets with rolling and recrystallization textures. *Comput. Mater. Sci.* 67, 424–433. <https://doi.org/10.1016/j.commatsci.2012.08.015>.
- Saai, A., Westermann, I., Dumoulin, S., Hopperstad, O.S., Berstad, T., 2011b. Influence of microstructure and texture on the bendability of AA7108 aluminium alloy. In: *Proceedings of the 10th International Conference on Technology of Plasticity*. ICTP, pp. 901–905. <https://doi.org/10.1007/s12289-015-1233-z>.
- Shifler, D.A., 2005. Understanding material interactions in marine environments to promote extended structural life. *Corros. Sci.* 47, 2335–2352. <https://doi.org/10.1016/j.corsci.2004.09.027>.
- Sozen, S., Guler, M., 2011. Determination of displacement distributions in bolted steel tension elements using digital image techniques. *Opt. Lasers Eng.* 49 <https://doi.org/10.1016/j.optlaseng.2011.07.002>, 1428–143.
- Suo, H., Cheng, H., Liang, B., Deng, K., Luo, B., Zhang, K., Chen, H., 2021. The mechanical degradation mechanism of CFRP/Al double-lap bolted joints (with and without corrosion protections) after seawater ageing. *Compos. Struct.* 276, 114561 <https://doi.org/10.1016/j.compstruct.2021.114561>.
- Talebi-Ghadikolaee, H., Naeini, H.M., Mirnia, M.J., Mirzai, M.A., Gorji, H., Alexandrov, S., 2020. Ductile fracture prediction of AA6061-T6 in roll forming process. *Mech. Mater.* 148, 103498 <https://doi.org/10.1016/j.mechmat.2020.103498>.
- Vargel C. Corrosion of aluminium (2004) Chapter B.3. Galvanic Corrosion. DOI: [10.1016/B978-0-08-044495-6.X5000-9](https://doi.org/10.1016/B978-0-08-044495-6.X5000-9).
- Zhang, B., Wang, J., Yan, F., 2018. Load-dependent tribocorrosion behaviour of nickel-aluminium bronze in artificial seawater. *Corros. Sci.* 131, 252–263. <https://doi.org/10.1016/j.corsci.2017.11.028>.
- Zhang, J., Ebrahimi, N., Lai, D., 2019. Galvanic corrosion risk of using galvanized A325 bolts in corrosion-resistant steel bridges. *J. Bridge Eng.* 24, 6.
- Zhang, Y., Yin, X., Yan, F., 2015. Effect of halide concentration on tribocorrosion behaviour of 304SS in artificial seawater. *Corros. Sci.* 99, 272–280. <https://doi.org/10.1016/j.corsci.2015.07.017>.